

Deep Submillimeter and Radio Observations in the SSA22 Field. IV. Spectral Energy Distributions, Star Formation Histories, and the Infrared-Radio Correlation of the 850 μ m-selected SMGs

XIN ZENG ,^{1,2} YIPING AO ,^{1,2} KEN MAWATARI ,^{3,4} AND HIDEKI UMEHATA ,^{5,6}

¹*Purple Mountain Observatory, Chinese Academy of Sciences, Nanjing 210023, China*

²*School of Astronomy and Space Sciences, University of Science and Technology of China, Hefei 230026, China*

³*Waseda Research Institute for Science and Engineering, Faculty of Science and Engineering, Waseda University, 3-4-1 Okubo, Shinjuku, Tokyo 169-8555, Japan*

⁴*Department of Pure and Applied Physics, School of Advanced Science and Engineering, Faculty of Science and Engineering, Waseda University, 3-4-1 Okubo, Shinjuku, Tokyo 169-8555, Japan*

⁵*Department of Physics, Graduate School of Science, Nagoya University, Furocho, Chikusa, Nagoya 464-8602, Japan*

⁶*Institute for Advanced Research, Nagoya University, Furocho, Chikusa, Nagoya 464-8602, Japan*

ABSTRACT

We analyze the spectral energy distributions (SEDs), star formation histories (SFHs), and infrared-radio correlation (IRRC) of 221 850 μ m-selected submillimeter galaxies (SMGs) in the SSA22 deep field. The average SEDs reveal that SMGs have cooler dust temperatures than local ULIRGs or starburst systems, and that higher-redshift SMGs tend to be more luminous and exhibit warmer dust. The median mass-weighted age is 567 Myr. Most galaxies in our sample began forming ~ 1.68 Gyr after the Big Bang, entered the ‘SMG phase’ after ~ 1 Gyr of evolution—when they are predominantly observed—and largely transitioned out of the ‘SMG phase’ to become quiescent within an additional ~ 0.2 Gyr. A subset of massive galaxies shows rapid early assembly with high star formation efficiencies (~ 0.2 -0.8). The majority of SMGs reside at the high-mass end of the star-forming main sequence, with a characteristic stellar mass of $M_{\text{star}} \sim 10^{11} M_{\odot}$, above which galaxies are predominantly either on the main sequence or already quenched. We observe a downsizing trend: more massive galaxies tend to ‘mature’ earlier, completing their major episodes of star formation at higher redshifts compared to lower-mass systems. Our sample contributes $\sim 21\%$ (28%) to the cosmic star formation rate density (stellar mass density), including the overdensity, with its relative contribution peaking at 50-60% in the redshift range $z = 2.5 - 3.5$. We suggest that 850 μ m surveys may miss a population of faint, warm galaxies at $z \lesssim 1 - 2$. The median infrared-radio correlation parameter q_{IR} is 2.37, evolving as $(1 + z)^{-0.11}$, likely due to AGN contributions at high redshift and intrinsic differences between low- and high-redshift populations.

Keywords: Submillimeter astronomy (1647), Ultraluminous infrared galaxies (1735), Galaxy formation (595), High-redshift galaxies (734)

1. INTRODUCTION

Massive galaxies at high redshift serve as key probes for tracing the history of cosmic star formation. Following the epoch of cosmic reionization, starbursts embedded in dense clouds gradually became the dominant component of cosmic star formation, contributing approximately 50-80% of the star formation rate density

(SFRD) (Hughes et al. 1998; Zavala et al. 2021). We focus on a key population of such systems: SMGs—high-redshift, massive, dust-obsured star-forming galaxies. Thanks to the negative k -correction at (sub)millimeter wavelengths, SMGs provide a uniquely powerful window into the early universe. They not only constitute a major component of cosmic star formation at early epochs but also offer critical insights into fundamental astrophysical questions: When and how did galaxies and stars first form? What are their evolutionary pathways? How was the universe enriched with metals over

time? Moreover, SMGs serve as vital laboratories for studying galaxy assembly, dynamical evolution, and the emergence of large-scale structure.

SMGs are ultra-luminous, dust-enshrouded star-forming galaxies, widely regarded as progenitors of local ellipticals (Genzel et al. 2003; Simpson et al. 2014, 2017; Lim et al. 2020a; Zhang et al. 2022). Sources selected at $850\ \mu\text{m}$ with flux densities $\gtrsim 1\ \text{mJy}$ —having a median of $\sim 4\ \text{mJy}$ —exhibit star formation rates (SFRs) ranging from tens to thousands of solar masses per year, with stellar masses typically in the range of $\sim 10^{10\text{--}12}\ M_{\odot}$ (Swinbank et al. 2014; Cunha et al. 2015; Dudzevičiūtė et al. 2020). They reside in massive dark matter halos of $\gtrsim 10^{13} h^{-1} M_{\odot}$ (Chen et al. 2016; An et al. 2019; Lim et al. 2020b) and are frequently found in association with cosmic large-scale structures (Dressler 1980; Tamura et al. 2009; Arrigoni Battaia et al. 2018; Uematsu et al. 2019; Zhang et al. 2024, 2025).

Approximately half of the energy from cosmic star formation is channeled through the cosmic far-infrared background (Dole et al. 2006), to which SMGs contribute significantly (Geach et al. 2017). However, single-dish submillimeter/millimeter surveys are limited by confusion noise and sensitivity, typically resolving only 10-40% of the cosmic infrared background (Wang et al. 2017; Gao et al. 2024). Next-generation facilities such as the 15-meter Xue-shan-mu-chang SubMillimeter Telescope (XSMT-15m; XSMT Project Collaboration Group et al. 2025) are expected to substantially improve constraints on the background radiation and cosmic SFRD.

In the local universe, ultra-luminous infrared galaxies (ULIRGs) are almost exclusively merger-driven systems (Lonsdale et al. 2006; Geach et al. 2017). By analogy, it was long assumed that high-redshift SMGs are similarly triggered by gas-rich major mergers (Toft et al. 2014), consistent with their often asymmetric morphologies, clumpy structures, and kinematically disordered gas motions (Alaghband-Zadeh et al. 2012; Menéndez-Delmestre et al. 2013). However, alternative models propose that SMGs can be sustained over longer timescales through steady cold gas accretion (Narayanan et al. 2015; McAlpine et al. 2019). Indeed, spatially resolved spectroscopy has revealed rotationally supported disks in many SMGs (Genzel et al. 2011; Swinbank et al. 2011; De Breuck et al. 2014; Barro et al. 2017), and their optical/far-infrared morphologies are often well described by exponential disk profiles (Targett et al. 2013; Hodge et al. 2016; Fujimoto et al. 2018). Recent high-resolution JWST observations further suggest that many SMGs may be massive, isolated disk galaxies whose intense star formation is driven by gravita-

tional instabilities in gas-rich disks (Gillman et al. 2023, 2024; Le Bail et al. 2024; Chan et al. 2025; Hodge et al. 2025; Zhang et al. 2025). Cosmological simulations also support the possibility of SMG-like systems evolving in isolation (Davé et al. 2010, 2011).

Since their discovery, SMGs have been considered likely progenitors of local elliptical galaxies due to their extreme infrared luminosities (Hughes et al. 1998; Eales et al. 1999; Lilly et al. 1999). In the ALMA era, dynamical mass estimates, luminosity evolution, and number densities have reinforced this view, indicating that SMGs possess the necessary properties to evolve into present-day early-type galaxies (Swinbank et al. 2006; Simpson et al. 2014). Compact quiescent galaxies at $z \sim 2$ share similar stellar masses, velocity dispersions, dynamical masses, sizes, and clustering properties with SMGs (Toft et al. 2014), and given the short duration of the SMG phase (\sim one to few 100 Myr), these quiescent systems are widely interpreted as the “evolutionary bridges” between SMGs and local ellipticals. However, such an evolutionary path would require significant structural transformation (Chen et al. 2015). To reconcile this, Barro et al. (2013) and Dekel & Burkert (2013) proposed an evolutionary sequence wherein early star-forming galaxies undergo compaction via violent disk instabilities or major mergers, followed by quenching through gas exhaustion, stellar feedback, and AGN activity, and finally puff up via dry minor mergers. At $z \lesssim 2$, galaxies may instead quench via morphological quenching or halo quenching, evolving directly into extended quiescent systems—though even in this scenario, without requiring a compact precursor phase.

An open and intriguing question remains: could a non-negligible fraction of SMGs retain their disk structure and evolve into present-day massive disk galaxies? Observational and theoretical studies suggest that galaxies undergoing major merger events that dramatically alter their structure can subsequently reform disk-like configurations. Simulations indicate that if the merging system remains gas-rich, a rotationally supported disk can re-emerge within a few Gyrs (Barnes 2002; Springel & Hernquist 2005; Robertson et al. 2006; Hopkins et al. 2009). Moreover, Governato et al. (2009) emphasized the role of environment, showing that even gas-poor merger remnants can regenerate disks through the accretion of cold streams from the cosmic web or cooling flows from hot halo gas. The model of Barro et al. (2013) also supports this view, suggesting that galaxies can rebuild disk structures via gas-poor mergers or dynamic instabilities prior to final quenching. Additionally, Gillman et al. (2024) found that the stellar disks of SMGs can remain intact and persist until at least $z \sim 1$. An equally

intriguing question is whether SMGs that avoid major disruptive events might retain their disk morphology to the present day. Future studies of massive quiescent discs at $z \sim 1$ -2 will be essential to address this possibility and refine our understanding of SMG long-term evolutionary pathways.

The concept of the “main sequence” of galaxies was first introduced by [Noeske et al. \(2007a\)](#) based on an analysis of approximately 3000 mass-selected field galaxies in the EGS deep field, revealing a robust and tight correlation between star formation rate (SFR) and stellar mass that evolves with redshift. [Daddi et al. \(2007\)](#) similarly discovered the $\text{SFR}-M_{\text{star}}$ main sequence relation in 24 μm -selected galaxies. [Davé et al. \(2011\)](#) proposed that this main sequence arises from a self-regulating equilibrium process between galactic star formation and the surrounding gas supply, where feedback mechanisms maintain a balance between gas accretion, star formation, and outflow processes.

During the 1970s and 1980s, a remarkably tight linear correlation between infrared and radio luminosities across several orders of magnitude was discovered in galaxies ([Helou et al. 1985](#); [Condon 1992](#); [Delhaize et al. 2017](#)), known as the infrared–radio correlation (IRRC), commonly characterized by the parameter q_{IR} . Although its precise physical origin remains debated, the IRRC is generally attributed to both emissions tracing star formation activity ([Ivison et al. 2010](#)). Ultraviolet radiation from young stars is reprocessed by dust into infrared emission, while relativistic electrons (Cosmic-Ray electrons) accelerated by supernova remnants of massive stars produce synchrotron radiation ([Condon 1992](#)). This correlation persists across diverse environments from galaxy clusters to field galaxies, and from the local universe to high redshifts, being observed in normal star-forming galaxies, luminous starbursts ([Helou et al. 1985](#)), and even AGN ([Morić et al. 2010](#)). And the IRRC does not evolve significantly with the galaxy’s distance from the main sequence ([Magnelli et al. 2015](#)). Due to its robustness, the IRRC has become a valuable tool for identifying radio-loud AGN, estimating star formation rates from radio luminosities, and determining distances to high-redshift galaxies ([Delhaize et al. 2017](#)).

The persistence of the IRRC at high redshifts presents a theoretical challenge, given the rapidly increasing energy density of the cosmic microwave background (CMB) with redshift ($U_{\text{CMB}} \propto (1+z)^4$) ([Murphy 2009](#)). Under these conditions, inverse Compton (IC) scattering and ionization losses should dominate cosmic-ray (CR) electron cooling, surpassing synchrotron radiation. This could potentially breakdown the IRRC at high redshift, or equivalently, increase q_{IR} with redshift ([Magnelli et al.](#)

2015). However, observations indicate that IC cooling has not yet overtaken synchrotron cooling at least up to $z \sim 2$ ([Magnelli et al. 2015](#)). Our sample demonstrates that the IRRC persists at least out to $z \sim 4$, and [Delhaize et al. \(2017\)](#) report that galaxies continue to follow the IRRC even at higher redshifts ($z \sim 6$). What mechanisms preserve the IRRC at high redshifts? Theoretical models suggest that enhanced galactic magnetic fields could increase the efficiency of synchrotron cooling, compensating for the increased energy losses from IC scattering and ionization due to the stronger CMB ([Sargent et al. 2010a](#); [Yoon 2024](#)). However, magnetic field amplification alone may be insufficient, as it would require extremely high field strengths. Moreover, under such conditions, CR electrons primarily lose energy via ionization and bremsstrahlung rather than synchrotron emission, which would further suppress non-thermal radio emission. Alternative explanations include the possibility that AGN activity dominates the radio emission at high redshifts, thereby maintaining the observed IRRC ([Murphy et al. 2009](#)), and/or enhanced free-free (bremsstrahlung) emission at high redshifts supplement the total radio luminosity ([Murphy et al. 2009](#); [Magnelli et al. 2015](#); [Delhaize et al. 2017](#)). A combination of these mechanisms is likely responsible for maintaining the correlation in the early universe.

This paper is organized as follows. In Section 2, we briefly describe the submillimeter and multi-wavelength data in the SSA22 deep field. In Section 3, we present the average SED of SMGs in the SSA22 field. We examine how the SEDs vary across different physical groupings of SMGs and detail the mean emission contributions from individual physical components. In Section 4, we present a detailed analysis of SMGs, focusing on their position relative to the star-forming main sequence, their specific star formation rates (sSFR), their lifetimes, and their contributions to the cosmic star formation rate density and stellar mass density (SMD). Finally, in Section 5, we investigate the infrared–radio correlation in SMGs, presenting the distribution and redshift evolution of the correlation parameter q_{IR} , as well as the relationship between submillimeter and radio flux densities.

Throughout this work, we adopt the cosmological parameters $H_0 = 70 \text{ km s}^{-1} \text{ Mpc}^{-1}$, $\Omega_\Lambda = 0.70$, and $\Omega_m = 0.30$. A [Chabrier \(2003\)](#) initial mass function (IMF) is assumed. Where necessary, quantities from the literature based on other IMFs have been converted to the Chabrier IMF: values derived with the [Salpeter \(1955\)](#) IMF are multiplied by 0.63 for SFR and 0.61 for stellar mass, while those based on the [Kroupa & Weidner \(2003\)](#) IMF are scaled by 0.94 for SFR and 0.92

for stellar mass (Madau & Dickinson 2014; Lim et al. 2020a).

2. DATA

We present the deepest 850 μm imaging of the SSA22 deep field to date, combining data from the SCUBA-2 Cosmology Legacy Survey (S2CLS; Geach et al. 2017) with additional observations of the central region (Ao et al. 2017). The total integration time amounts to 91 hours, covering an area of 0.34 deg², with a central sensitivity reaching $\sigma_{850} \sim 0.79 \text{ mJy beam}^{-1}$. The JVLA 3 GHz observations of the central area of SSA22 field were conducted in 2015 and 2016, achieving a sensitivity of 1.5 $\mu\text{Jy beam}^{-1}$ (before primary beam correction) and an angular resolution of 2''.3 \times 2''.0. For detailed descriptions of the SCUBA-2 850 μm observations and data reduction, we refer readers to Paper II of this series (Zeng et al. 2024); for the radio observations and data processing, see Paper I (Ao et al. 2017) and III.

Due to the inhomogeneous coverage of multiwavelength data, we perform source identification within a 0.27 deg² area of the SSA22 field. We ultimately identify 248 SMG candidates using four complementary identification methods based on multiwavelength data: radio (JVLA) sources, 24 μm (*Spitzer*/MIPS) sources, 8 μm (*Spitzer*/IRAC) sources, and optical/NIR red colors. We then estimate their photometric redshifts and derive physical properties through spectral energy distribution (SED) fitting, employing EAZY (Brammer et al. 2008) for photo- z estimation and CIGALE (Boquien et al. 2019) for full SED modeling. After applying quality cuts based on the SED fitting results, our final sample comprises 221 robust SMGs. For details on the multiwavelength dataset, source identification, and SED fitting methodology, we refer the reader to Paper III.

3. THE AVERAGE SED OF SSA22 SMGS

In this section, we analyze the average SED of SMGs derived from the best-fit CIGALE models, compare our results with literature findings (Section 3.1), and discuss their SED variations across different redshifts and dust masses (Section 3.2) along with the radiation components of SMGs (Section 3.3). The average SEDs of the SSA22 SMGs are available in the supplementary material.

3.1. Average SED

Following the methodology of Dudzevičiūtė et al. (2020), we normalized the SEDs of all 221 SMGs to a median infrared luminosity of $L_{\text{IR}} = 2.25 \times 10^{12} \text{ L}_{\odot}$ and computed the median flux at each wavelength to construct the average SED.

As shown in Figure 1 image (a), the composite SED exhibits significant variations across different spectral regimes. At wavelengths $\gtrsim 100 \mu\text{m}$, the cold dust emission produces a broadly consistent spectral shape, though the far-infrared peak wavelength varies considerably due to differences in dust temperature, resulting in a relatively flat average spectrum with a slight peak at 60-70 μm . Between 3-100 μm , the SEDs show ~ 0.5 dex scatter, primarily driven by variations in star formation-heated dust and polycyclic aromatic hydrocarbons (PAHs) emission. The ultraviolet-to-near-infrared (UV-to-NIR) regime displays even greater diversity (3-5 orders of magnitude), likely reflecting substantial differences in geometry, star formation activity, dust mass, and distribution—factors that complicate the optical/NIR detection of SMGs, particularly when combined with cosmological dimming effects due to k -correction at high redshifts (Dudzevičiūtė et al. 2020).

Color-coding the SEDs by V-band dust attenuation (A_V) reveals that SMGs with different attenuation levels can exhibit similar SED shapes. For instance, a highly obscured galaxy (due to edge-on orientation or compact dust distribution) with vigorous star formation may have an SED comparable to that of a less obscured system. This degeneracy between A_V , stellar radiation, and dust temperature underscores the diversity of SMG physical properties.

Comparison with the ALESS (Cunha et al. 2015) and AS2UDS (Dudzevičiūtė et al. 2020) samples (normalized to our mean infrared luminosity) shows broad agreement within 1σ uncertainties (Figure 1 panel (b)). Dudzevičiūtė et al. (2020) noted that the ALESS sample lacks highly dust-obscured sources, leading to relatively moderate dust attenuation on average. This may explain why ALESS galaxies show stronger stellar emission. Similarly, we suggest that the SSA22 sample either has less dust attenuation or contains more young and old stellar populations, resulting in enhanced emission from the ultraviolet to near-infrared. Between 3-30 μm , our sources exhibit PAH emission that is 1-4 times stronger than that shown in the literature. This may be due to a higher PAH mass fraction assumed in our models or a larger fraction of hot dust (set to $\sim 10\%$) associated with star-forming regions. However, it is more likely attributable to insufficient mid-infrared observations leading to modeling biases. Consequently, our average SED shows weaker cold dust emission at $\sim 100 \mu\text{m}$ compared to ALESS/AS2UDS. Alternatively, this difference could stem from variations in the dust models used in CIGALE and MAGPHYS, or from the greater diversity of SMGs in SSA22, which exhibit a wider range of dust temperatures. Consequently, the far-infrared peak wavelengths

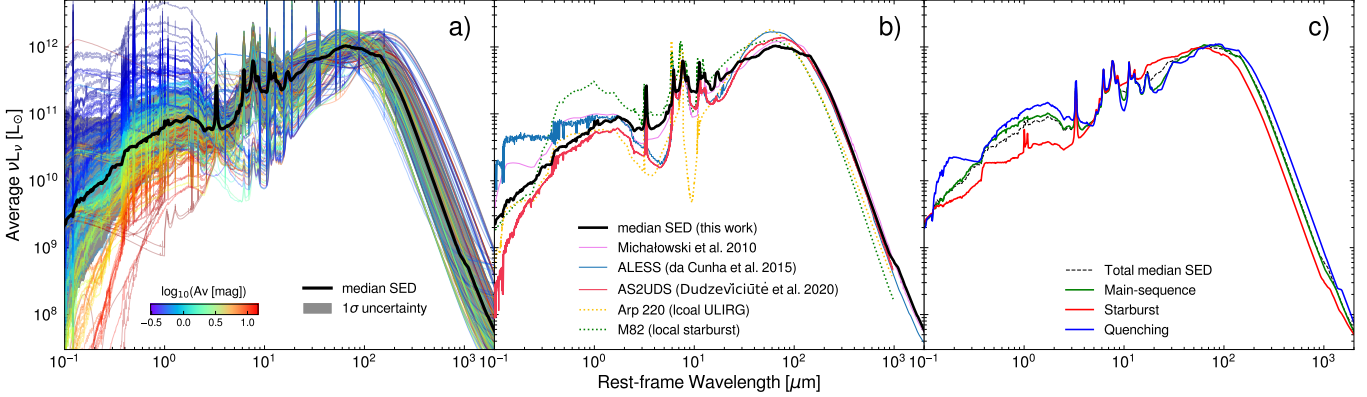


Figure 1. Panel (a): The SEDs of the 221 SMGs in the SSA22 deep field, normalized to the average infrared luminosity, and color-coded by dust attenuation A_V . The solid black line and grey shaded gray region represent the median SED and 1σ dispersion, respectively. Panel (b): A comparison of the SSA22 SMG SEDs with those from other submillimeter surveys and local starburst galaxies and ULIRGs. Our results are consistent with the literature and exhibit colder dust temperatures than typical local ULIRGs or starbursts. However, the SED shape of SMGs more closely resembles that of local ULIRGs than that of local starbursts. Panel (c): SEDs of SMGs in different evolutionary stages. Quiescent SMGs display colder dust temperatures and prominent features associated with older stellar populations, while starbursting SMGs show stronger dust attenuation and warmer dust temperatures.

vary significantly, resulting in a flatter average SED in this region. At longer wavelengths, the emission from colder dust remains consistent.

Comparisons with local ULIRGs and starburst galaxies, represented by Arp220 and M82, reveal distinct features: local starbursts show stronger stellar emission ($< 5 \mu\text{m}$) and hotter dust continua with prominent PAH features due to the heat by nearby starburst activity (5-30 μm) (Menéndez-Delmestre et al. 2009). ULIRGs exhibit deeper 9.7 μm silicate absorption and warmer dust temperatures than SMGs. Crucially, Menéndez-Delmestre et al. (2009) also pointed out that SMGs are not direct high-redshift analogs of local starbursts or ULIRGs, spatial extent of star formation region in SMGs is significantly larger than in the local starbursts or ULIRGs. However, as noted by Cunha et al. (2015) and Dudzevičiūtė et al. (2020), local ULIRGs provide better templates for high-redshift SMGs ($z \gtrsim 2.5$) than starburst systems like M82.

Assuming a simple blackbody model, we estimate the characteristic dust temperature (T_{peak}) from the peak wavelength of the average SED using Wien's displacement law (Uematsu et al. 2024). When using flux densities in units of [mJy] measured at discrete frequencies, the peak temperature is given by $T_{\text{peak}}[\text{K}] = 5099/\lambda_{\text{peak}}[\mu\text{m}]$. Arp220 and M82 exhibit emission peaks at $\sim 70\text{-}90 \mu\text{m}$, corresponding to $T_{\text{peak}} \approx 60\text{-}70 \text{ K}$. In contrast, the SSA22 and AS2UDS samples, along with the sample from Michałowski et al. (2010), exhibit cooler dust temperatures around 50 K ($\lambda_{\text{peak}} \sim 100 \mu\text{m}$). The ALESS sample falls between these values, with a temperature of approximately 60 K.

This systematic trend reveals that SMGs harbor significantly cooler dust than local ULIRGs or starburst systems, aligning with Symeonidis et al. (2013)'s finding of cooler dust in low-redshift (U)LIRGs compared to their local counterparts. Simpson et al. (2017); Dudzevičiūtė et al. (2020) further demonstrate that 870 μm -selected AS2UDS SMGs preferentially detect colder systems, with dust temperatures $\sim 7\text{-}8 \text{ K}$ lower than low-redshift (U)LIRGs at comparable luminosities (Simpson et al. 2017). Symeonidis et al. (2013) attribute this to increasing dust mass and/or physical extent of (U)LIRGs with redshift, a interpretation supported by Menéndez-Delmestre et al. (2009)'s finding that SMGs have more spatially extended dust distributions than local ULIRGs.

Figure 1 (c) illustrates systematic variations in the SEDs of SMGs at different evolutionary stages. Quiescent SMGs—defined as those lying more than a factor of 3 below the star-forming main sequence (see Section 4.1)—exhibit cooler dust temperatures and show clear signatures of older stellar populations, including a prominent 1.6 μm stellar bump and stronger Balmer/4000Å breaks. Additionally, an elevation in far-ultraviolet flux is observed, likely resulting from the buildup of low-mass post-AGB stars (Bruzual & Charlot 2003). In contrast, starbursting SMGs (with SFRs exceeding 3 times the main-sequence value) are characterized by stronger dust attenuation and warmer dust temperatures.

3.2. SED Variations Across Bins

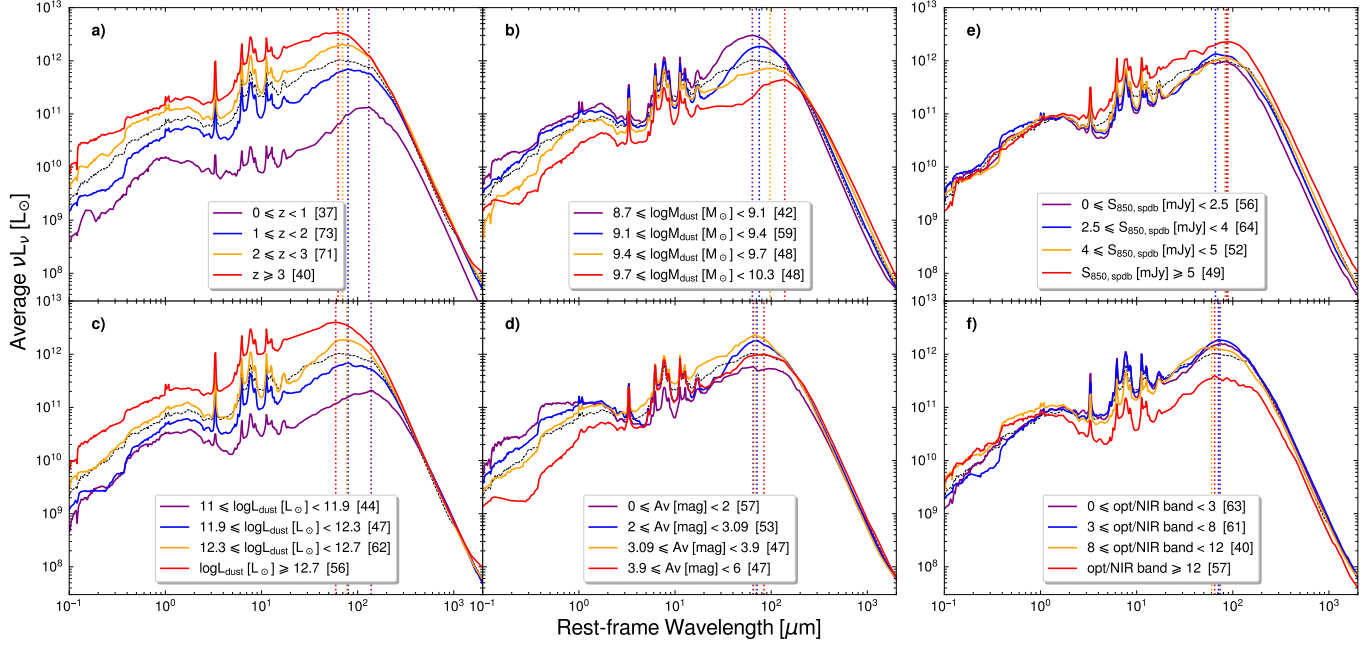


Figure 2. The median SEDs for SMGs for groups categorized by different physical or observational properties. The number of sources in each group shown within brackets in the legend. The black dashed curve represents the median SED of the total sample, while vertical dotted lines indicate the peak of FIR emission for each group’s SED. Notably, the average SEDs within each group are not normalized to their infrared luminosity.

We grouped the SSA22 SMGs according to various physical and observational properties and computed the average SED for each group. To clearly highlight differences, the average SEDs are not normalized to infrared luminosity.

Figure 2 panel (a) shows the average SMG SEDs in different redshift bins. Compared to higher-redshift sources, low-redshift SMGs ($z < 1$) exhibit younger stellar populations, with relatively bluer UV-optical emission, weaker dust attenuation and metal absorption features, and reduced thermal dust and PAH emission, resulting in fainter submillimeter fluxes and luminosities. Figure 2 panel (a) shows significant differences in average luminosity among SMGs at different redshifts, which may be partly due to biases introduced by the dependence of SED fitting on far-infrared (FIR) data (Swinbank et al. 2014; Dudzevičiūtė et al. 2020). As redshift increases, the total SED luminosity rises and the far-infrared peak shifts to shorter wavelengths, equally increasing characteristic dust temperature.

For the results presented above and in the following sections, we should bear in mind several potential biases that may affect their interpretation. First, SED fitting relies on FIR band constraints. This introduces a selection bias toward intrinsically brighter sources at high redshifts, while low-luminosity galaxies at similar redshifts may fall below the FIR detection limit. Consequently, some studies argue that the ap-

parent luminosity evolution of SMGs is largely an artifact of this observational bias (Swinbank et al. 2014; Dudzevičiūtė et al. 2020). However, other works contend that such biases alone cannot fully account for the observed trends (Simpson et al. 2017; Zavala et al. 2018; Lim et al. 2020a). They suggest that infrared luminosity and dust temperature are still governed by underlying physical processes, with dust temperatures evolving with cosmic time (Symeonidis et al. 2013; Sommovigo et al. 2022; Viero et al. 2022; Mitsuhashi et al. 2024). In particular, a more fundamental correlation likely exists among infrared luminosity, dust temperature, and redshift (Symeonidis et al. 2013; Zavala et al. 2018). Second, bandpass selection effects play a significant role (see also Section 4.1 and Section 4.4). Observations at longer (sub)millimeter wavelengths are more sensitive to high-redshift dusty galaxies (Casey et al. 2014; Zavala et al. 2014; Wang et al. 2017), while 850 μ m surveys preferentially select galaxies with cooler dust temperatures (Chen et al. 2021). As a result, 850 μ m surveys are inherently incomplete for warm-dust systems and for galaxies at both low and very high redshifts. Moreover, uncertainties in the detection and physical characterization of high-redshift galaxies, combined with the intrinsic diversity of SMG populations, further complicate the interpretation. A full resolution of these issues lies well beyond the scope of this study. Readers should simply

be aware of these potential biases when evaluating our conclusions.

Figure 2 image (b) reveals that galaxies with higher dust mass have lower infrared luminosity, lower dust temperatures, and stronger submillimeter fluxes and luminosities. Cunha et al. (2015) noted that at a given luminosity, SMGs with lower 870 μm fluxes tend to have higher dust temperatures, while submillimeter flux is positively correlated with dust mass (Dudzevičiūtė et al. 2020). Qualitatively, dust mass and temperature exhibit an inverse correlation, so galaxies with lower dust mass tend to have higher dust temperatures (see Section 5.4 of Paper III or Figure 13 of Uematsu et al. 2024). Dust distribution or optical depth (i.e., compactness) may also influence dust temperature (Simpson et al. 2017; Dudzevičiūtė et al. 2020). However, since dust mass accumulation requires time, sources with lower dust mass are preferentially found at higher redshifts, contributing to their higher luminosities. We find no clear trend in SED properties with stellar mass. SMGs with higher stellar mass tend to show stronger emission from both young and old stellar populations and redder stellar continua, but this trend is not strict. Furthermore, thermal dust, PAH, and cold dust emission do not exhibit systematic variations with stellar mass.

Figure 2 plot (c) displays the average SEDs in different dust luminosity bins. As dust luminosity increases, the dust emission peak shifts to shorter wavelengths, thermal dust emission strengthens, and the stellar continuum becomes steeper. Due to strong k -corrections, submillimeter fluxes show little variation across different infrared luminosity bins.

As V-band attenuation increases (Figure 2 (d)), the stellar continuum of SMGs becomes progressively fainter and steeper, while dust emission intensifies overall and PAH features become more prominent. However, the trends of dust temperature and submillimeter flux with A_V are weak, showing only minor differences in the highest extinction bin. Unlike dust mass, A_V does not strongly correlate with dust temperature, suggesting that A_V is governed by multiple factors rather than a single dominant process—such as galaxy inclination, dust mass, and geometric distribution of dust. Cunha et al. (2015) argued that due to dust isotropy, galaxy inclination increases extinction without significantly altering the shape of dust emission. The differences in average SEDs may arise from variations in source compactness. In galaxies with more compact dust distributions, the higher dust column density and dust located closer to the stars experience a stronger radiation field, enhancing the efficiency of converting stellar radiation into dust emission.

This paints an evolutionary picture: as intense star formation proceeds, large amounts of dust are produced, UV photons from young stars are absorbed, and dust thermal emission strengthens. Coupled with increasing dust column density, the efficiency of dust radiation improves. Generally, galaxies with more vigorous star formation exhibit stronger infrared emission and hotter dust temperatures. However, at a fixed star formation rate, as dust accumulates, the efficiency of heating the outer dust layers decreases, leading to lower infrared luminosity and gradually cooler average dust temperatures. This process also enhances submillimeter emission.

In Figure 2 (e), we divided the SMG sample into bins according to their deblended 850 μm flux density, with approximately equal numbers of sources per bin. The median redshifts of the groups are similar but increase slightly with flux: 1.79, 1.90, 2.03, and 2.10. Brighter SMGs tend to lie at higher redshifts (see also Section 5.1 in Paper III). Aside from the brightest group, which shows significantly higher infrared luminosity, the overall SEDs across submillimeter flux bins are quite similar. Cunha et al. (2015) also found similar SEDs across flux levels and suggested that redshift and negative k -correction may allow intrinsically similar sources to appear at different fluxes, resulting in comparable uncertainties across groups. Thus, the 850 μm flux alone cannot distinguish between galaxies with different physical properties within the SMG sample. Conversely, this implies that our average SED (Figure 1) adequately represents the overall population of SCUBA-2 850 μm –selected galaxies in the SSA22 field. We observe that sources with fainter 850 μm flux have relatively brighter stellar luminosity and less dust attenuation (flatter stellar continuum). As noted earlier, 850 μm flux correlates positively with dust mass; hence, fainter sources have less dust and lower dust mass fractions ($M_{\text{dust}}/M_{\star}$). Dust masses in the flux bins are 0.94, 1.42, 2.17, and $3.77 \times 10^9 M_{\odot}$, with corresponding dust mass fractions of $\sim 0.6\%$, 0.9% , 1.3% , and 2.4% . Additionally, at similar luminosities, fainter galaxies, having less dust, exhibit higher relative dust heating efficiency. As Cunha et al. (2015) pointed out, there is an inverse correlation between submillimeter flux and dust temperature: lower 850 μm flux corresponds to relatively hotter dust.

In Figure 2 (f), SMGs are grouped by the number of available optical/NIR bands. As expected, optically brighter sources (those with more available bands) show higher optical luminosity and less dust attenuation. The median A_V values for sources from optically faint to bright (fewest to most bands) are 3.87, 3.35, 3.09, and

1.72 mag, with corresponding median redshifts of 2.20, 2.05, 1.90, and 1.25. The SEDs of the first three groups are similar, while the fourth group differs significantly. This is likely because the group with the most available bands is dominated by much lower-redshift sources, which may be primarily composed of lower-mass SMGs, resulting in notably lower infrared luminosity. The median dust masses of the first three groups are 2.29, 2.14, and $1.52 \times 10^9 M_{\odot}$, with dust mass fractions all around $\sim 1\%$. However, optically faint SMGs exhibit higher dust attenuation, suggesting more efficient mechanisms for absorbing star formation radiation—such as more compact dust distributions (leading to higher column densities and extinction) and warmer stellar radiation field (Cunha et al. 2015), more intense star formation activity (Magnelli et al. 2014; Cowley et al. 2017), or a combination of both.

3.3. The radiation Composition of SMGs

Figure 3 exhibit the average SED of SSA22 SMGs and the average radiation composition.

In the UV-to-NIR regime, SMGs host vigorous star formation that produces abundant young stars. Their unattenuated stellar radiation includes strong UV emission, with comparable luminosity at 100 nm and 2 μm . However, the characteristic dust-rich nature of SMGs leads to substantial attenuation, with an average V-band extinction of 3.09 magnitudes. The UV portion of the spectrum also shows significant contributions from AGN activity.

The gas-rich environment of SMGs produces prominent spectral features, including the Lyman break at 91.1 nm and Lyman series absorption shortward of 121.6 nm.

The composite spectrum also exhibits clear Balmer/4000Å breaks - sensitive diagnostics of stellar population age, metallicity, and Lyman continuum escape fraction (Wilkins et al. 2023). The Balmer break primarily originates from A-type stars ($T_{\text{eff}} \sim 10000$ K), where hydrogen atoms efficiently populate the second energy level, creating bound-free absorption near 3646 Å (Salvato et al. 2018; Wilkins et al. 2023; Vikaeus et al. 2024). Dust attenuation enhances this feature (Vikaeus et al. 2024), while its evolution tracks stellar population age: it peaks in systems dominated by 0.3-1 Gyr stars, gets filled in by strong UV continuum from younger stellar population and nebular, and smooths out in older population (Bruzual & Charlot 2003; Vikaeus et al. 2024). The 4000 Å break, caused by metal absorption lines (e.g., Ca II H/K, G-band, various metal lines heavier than helium) in late-type stars (Bruzual & Charlot

2003), becomes more prominent in quiescent galaxies (H. Mo 2010; Dudzevičiūtė et al. 2020).

A near-universal feature in stellar spectra (except very young ~ 1 Myr populations) is the 1.6 μm bump, arising from minimum H^- opacity in cool stellar atmospheres. This feature proves particularly useful for photometric redshift estimation (Sawicki 2002).

While the origin of the 220 nm extinction bump remains debated, it has been attributed to PAH absorption (Fitzpatrick 1999; Shvai et al. 2022). Its absence in our SMG SEDs may result from spectral smoothing due to source diversity, or alternatively, reflect lower PAH abundances in high-redshift systems during early dust enrichment phases.

At 3 μm , dust emission becomes significant and begins to dominate over the radiation from older stellar populations in SMGs. The mid-infrared emission from SMGs consists of two primary components: thermal dust continuum and PAH/molecular emission features (Menéndez-Delmestre et al. 2009). The continuum emission at wavelengths $\gtrsim 12 \mu\text{m}$ originates from very small grains (VSGs; $\lesssim 10$ nm) heated to temperatures $\lesssim 250$ K in star-forming regions or near obscured AGN. In contrast, the $\lesssim 6 \mu\text{m}$ continuum arises from hotter dust ($\gtrsim 500$ K) located in AGN or compact starburst nuclei (Menéndez-Delmestre et al. 2009).

Between these regimes, the spectrum exhibits prominent PAH emission features excited by UV photons in star-forming regions. These nanometer-sized PAH molecules, composed of aromatic rings with attached hydrogen and trace elements (e.g., Si, Mg; Menéndez-Delmestre et al. 2009), produce characteristic vibrational bands at 3.3, 6.2, 7.7, 8.6, 11.3, 12.7, and 17 μm from C-C/C-H bond stretching and bending modes (Draine & Li 2007). The prominent absorption features at 9.7 and 18 μm arise from amorphous silicate grains (Dudzevičiūtė et al. 2020).

At longer wavelengths, $\gtrsim 100 \mu\text{m}$, the far-infrared emission transitions to larger, cooler dust grains. These grains reach thermal equilibrium in moderate radiation fields, emitting as modified blackbody with temperatures of 30-60 K (Casey et al. 2014; Boquien et al. 2019). The Rayleigh-Jeans tail at ~ 100 -1000 μm follows a ν^2 dependence modified by the dust emissivity index (typically 1.5-1.8), resulting in an overall $\nu^{3.5-3.8}$ flux decay. The modified blackbody model has become the standard approach for characterizing far-infrared dust emission in galaxies (Simpson et al. 2019; Dudzevičiūtė et al. 2020; Liao et al. 2024). This spectral shape, combined with negative k -correction, produces a remarkable observational advantage in the 500-3000 μm regime: galaxies of fixed intrinsic luminosity maintain nearly constant ob-

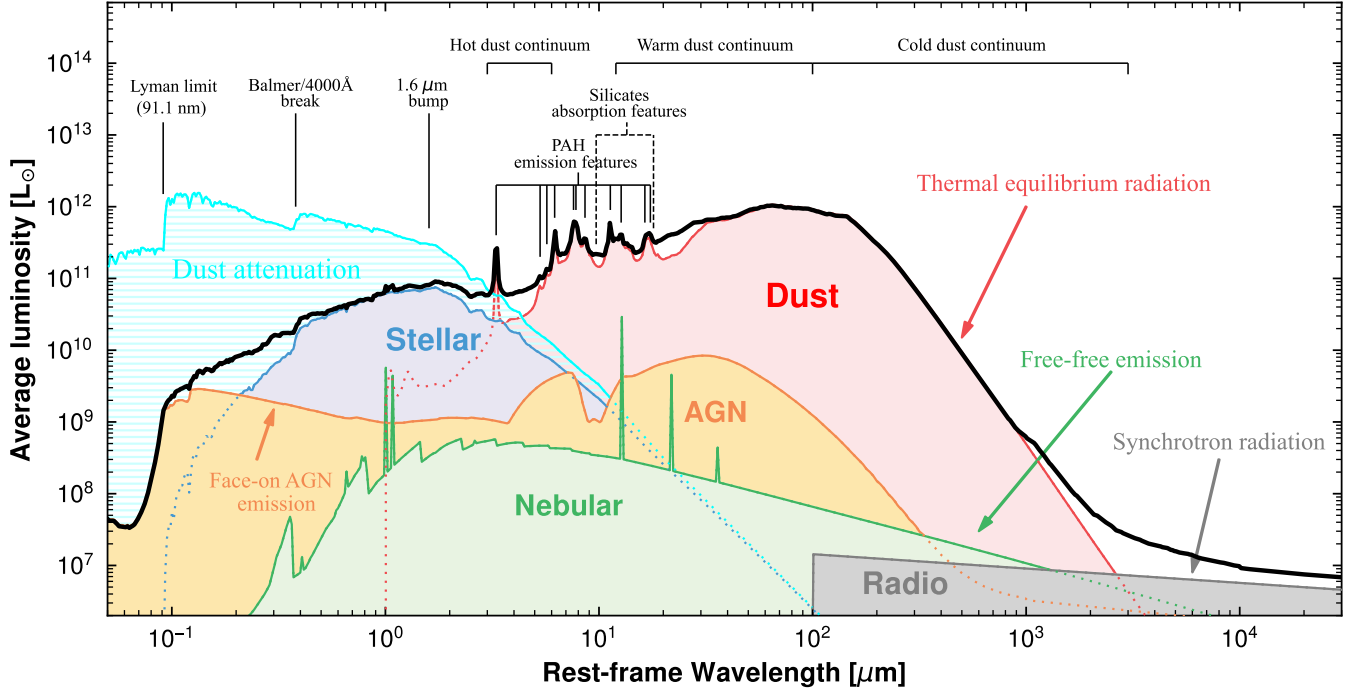


Figure 3. The average SED of SSA22 SMGs, along with the median contributions from various physical components. Different emission components—including stellar populations and dust features—are indicated with distinct colors and labels.

served flux densities across a wide redshift range ($z \sim 1$ -6) (Blain 2002). In fact, the negative k -correction causes galaxies observed at wavelengths longer than 1 mm to exhibit higher fluxes at higher redshifts. These properties make (sub)millimeter observations particularly effective for detecting high-redshift dusty galaxies.

The SED turnover at ~ 1 - 1.5 mm marks the transition where nebular emission and radio radiation begin to dominate over dust continuum. Nebular radiation primarily originates from thermal free-free emission in HII regions ionized by stellar UV photons. This bremsstrahlung process, which cools thermal electrons in unmagnetized plasmas, exhibits a characteristic flat spectrum (spectral index ~ -0.1) at low frequencies ($h\nu \ll kT$), becoming steeper at higher frequencies. As noted by Condon (1992), this emission becomes significant in the 30-200 GHz window where neither far-infrared nor radio continuum dominates.

The long-wavelength SED is governed by synchrotron radiation from relativistic electrons accelerated in supernova remnants of massive ($\gtrsim 8 M_\odot$) stars (Condon 1992). The power-law energy distribution of these electrons produces a corresponding power-law synchrotron spectrum with typical indices of 0.3-2.0. Studies of star-forming galaxies reveal a median spectral index of $\alpha \sim 0.8$ at rest-frame 1.3-10 GHz, flattening at lower frequencies due to free-free absorption and spectral aging from energy losses (An et al. 2021, 2024). Both the high-

and low-frequency of the radio spectrum become slightly steeper with increasing stellar mass, a trend that can be explained by age-related synchrotron losses, where cosmic-ray electrons lose energy over time (An et al. 2021). Massive stars have short lifetimes ($\lesssim 3 \times 10^7$ yr), and the lifetimes of relativistic electrons are also limited ($\lesssim 10^8$ yr), making radio emission a tracer of relatively recent star formation activity (Condon 1992). However, accurately observing and constraining the star formation activity in galaxies remains challenging. Although synchrotron radiation is highly directional due to the Doppler effect of relativistic electrons, the observed emission in galaxies typically originates from relatively “old” electrons ($\gtrsim 10^7$ yr), which have long since propagated far ($\gtrsim 1$ kpc) from their short-lived ($\gtrsim 10^5$ yr) supernova remnants. As a result, the original sites of electron acceleration have already disappeared, and their spatial distribution has been significantly smoothed out. Consequently, radio emission observed in galaxies appears diffuse across the entire galactic extent (Condon 1992).

Far-infrared–radio correlation has been observed in spiral galaxies, starburst nuclei in both galaxy cluster and blank field. This correlation is a general feature of galaxies undergoing intense star formation Helou et al. (1985). Although the exact origin of this correlation remains debated, a prevailing view holds that massive stars are the key factor Condon (1992), both radio and

far-infrared emissions trace star formation activity: far-infrared emission reflects dust heated by star formation, while radio emission traces synchrotron radiation from relativistic electrons in supernova remnants (Shim et al. 2022; Zavala et al. 2018).

AGN contribute across multiple wavebands, predominantly in the mid-infrared and radio (with additional contributions in the UV and optical for type-1 AGN). The AGN fraction in SMGs can reach $\sim 20\text{--}40\%$ or higher (Alexander et al. 2005; Laird et al. 2010; Johnson et al. 2013; An et al. 2019; Stach et al. 2019). However, studies have shown that at least $\sim 85\%$ of the far-infrared emission in SMGs is powered by star formation activity (Laird et al. 2010). In general, AGN contribute little to the total luminosity and even less to the far-infrared and millimeter emission of SMGs, typically $\lesssim 10\%$ (Johnson et al. 2013). As seen in our results, these findings are well supported.

4. THE STAR-FORMATION HISTORY

This chapter is organized according to the following logical structure: In section 4.1, we explore the relationship between SMGs and the star-forming main sequence, highlighting trends in specific star formation rate (sSFR) and the downsizing effect. Section 4.2 reports on the stellar mass assembly histories of SMGs, including a discussion of their characteristic ages and lifetimes. Section 4.3 quantifies the contribution of SMGs to the cosmic star formation rate density and stellar mass density (SMD). Finally, we presented a phenomenological picture of 850 μm -selected SMG evolution based on statistical results (Section 4.4), and briefly discussed the downsizing trend as well as the reasons why submillimeter surveys typically struggle to detect SMGs at $z \lesssim 1$.

4.1. Main-sequence of SMGs

Figure 4 presents the SFR– M_{star} distribution for SMGs across different redshift slices. We plot Speagle et al. (2014)’s main-sequence relation as a solid cyan line in the figure:

$$\log_{10} \text{SFR} = (0.84 - 0.026t) \times \log_{10} M_{\text{star}} - (6.51 - 0.11t), \quad (1)$$

where t is the age of the Universe in Gyr. The dotted lines indicating a 0.2 dex uncertainty, which represents the intrinsic 1σ scatter of the main sequence (Speagle et al. 2014).

We define the main sequence range as the region between $1/3$ and 3 times the main sequence SFR (red and black solid lines in figure 4, and see also left image of figure 5), encompassing approximately 2.5σ of the intrinsic

scatter. This means that if an SMG is located at a position three times above the main sequence (taking into account the SFR, M_{star} , and redshift of each source), we define it as a starburst system (Cunha et al. 2015; Barrufet et al. 2020; Shim et al. 2022). This criterion is adopted to facilitate comparisons with the literature. We note that this threshold is not strictly standardized; some studies use a factor of two (Elbaz et al. 2011; Aravena et al. 2020), while others adopt a factor of four (Dudzevičiūtė et al. 2020; Lim et al. 2020a). Similarly, SMGs lying more than three times below the main sequence are classified as quenched systems.

We can see that at early epochs ($z > 2.5$), SMGs are predominantly in either the starburst or main-sequence phase. The SSA22 protocluster is located at $z = 3.09$. Accounting for photometric redshift uncertainties, we associate sources within $z = 3.09 \pm 0.1$ with this large-scale structure and mark them with yellow stars. Some of these may be enhanced in activity due to environmental effects, while others could be undergoing accelerated (“over”) evolution as a result of the dense environment. At later times ($z \lesssim 2.5$), the most massive galaxies ($M_{\star} > 10^{11} M_{\odot}$) begin to quench, and the star formation activity among 850 μm -selected galaxies gradually becomes dominated by lower-mass systems.

Left image of figure 5 shows the offset of galaxies from the main sequence as a function of stellar mass. We identify a “characteristic mass” scale, $M_{\star} \gtrsim 10^{11} M_{\odot}$, above which SMGs are almost exclusively either on the main sequence or already quenched. In fact, nearly all quiescent SMGs lie above this threshold. Moreover, we find that more massive galaxies tend to “mature” earlier—consistent with the findings of Firmani & Avila-Reese (2010), who reported that the mass of galaxies in transition increases with redshift. Conversely, SMGs that undergo their starburst phase at later cosmic times tend to be less massive. This behavior aligns with the “downsizing” paradigm (Cowie et al. 1996): by $z \lesssim 2.5$, the most massive 850 μm -selected SMGs have already assembled the bulk of their stellar mass, and their star formation rates decline as they transition into quiescence. Consequently, the dominant contributors to dust-obscured star formation shift toward lower-mass galaxies at later epochs.

4.1.1. Evolutionary State of SMGs

Next, we examine in detail the fractions of 850 μm -selected SMGs in different evolutionary states and how these fractions evolve with redshift. However, we emphasize that—despite the negative k -correction at 850 μm , which renders our luminosity limit nearly constant ($\sim 10^{12} L_{\odot}$) across redshifts $z \sim 1 - 6$ for a fixed

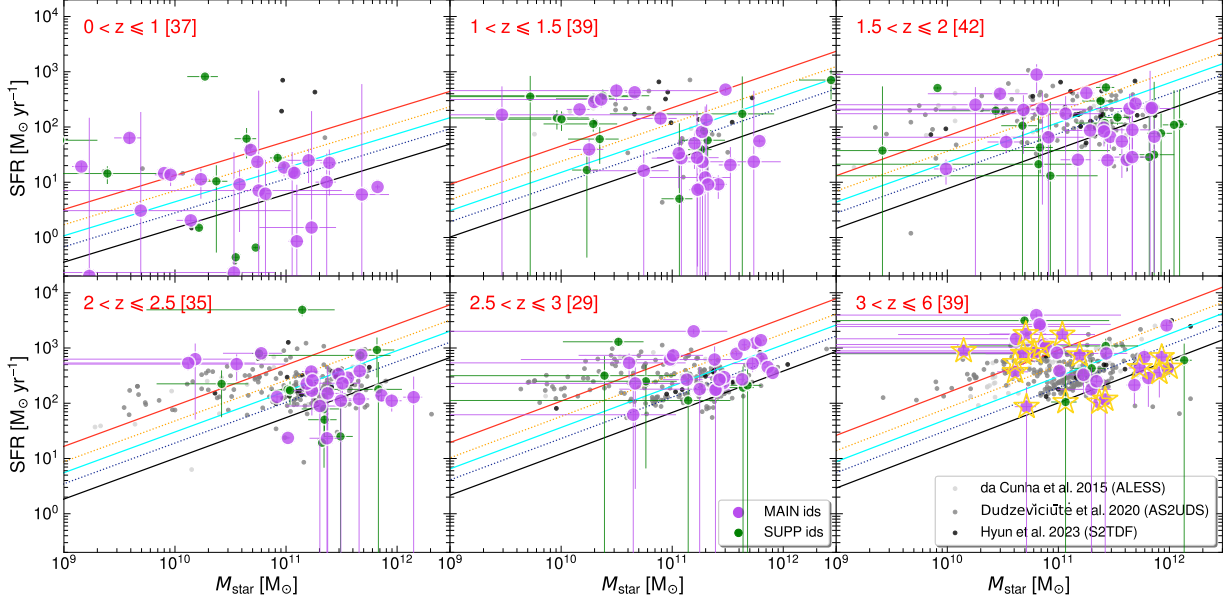


Figure 4. The distribution of SMGs on the SFR- M_{star} panel. The cyan solid line denotes the main sequence relation (Speagle et al. 2014) at the central value of the redshift range, with yellow and blue dashed lines representing the 1σ scatter (0.2 dex). The outermost red and black solid lines delineate the 2.5σ dispersion; SMGs within this boundary are considered main sequence galaxies, while those outside are classified as starburst or quiescent systems. Grey dots represent SMGs from ALMA surveys (Cunha et al. 2015; Dudzevičiūtė et al. 2020; Hyun et al. 2023). It's important to note that classification actually requires calculations based on individual galaxy redshifts and masses. Purple and green circles represent counterparts identified through different methods (see Paper III in the series), showing consistent distributions of SMGs across methods. Yellow stars indicate SMGs within the redshift range of 3.09 ± 0.1 , most of which remain on the main sequence or starburst phase.

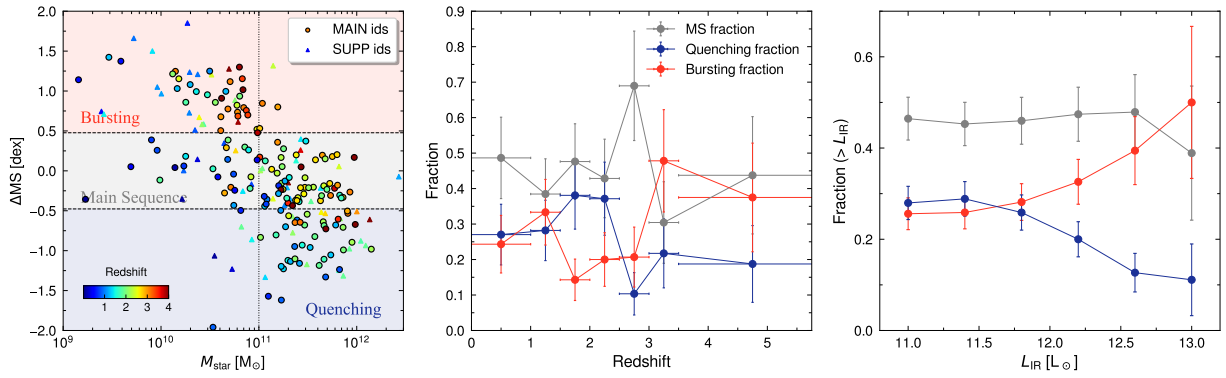


Figure 5. Left: The distribution of galaxies' offset ($\Delta\text{MS} = \log_{10}(\text{SFR}/\text{SFR}_{\text{MS}})$) from the main sequence against stellar mass. The horizontal dashed lines serve as a boundary between the main sequence and quiescent (or starburst) states. The vertical dashed line indicates a characteristic stellar mass $M_{\text{star}} \gtrsim 10^{11} M_{\odot}$; above this threshold, SMGs are predominantly quiescent or on the main sequence, while lower-mass systems tend to be starbursts or main-sequence galaxies. Circles and triangles denote counterparts identified through different methods (refer to Paper III in the series), showing broadly consistent distributions. Middle: Evolution of SMGs in different evolutionary stages with redshift. Right: Fraction of SMGs in different evolutionary stages, conditioned on exceeding a given luminosity threshold.

detection threshold—the $850 \mu\text{m}$ selection itself still introduces significant biases. For instance, $850 \mu\text{m}$ observations preferentially select galaxies with cooler dust temperatures (Chen et al. 2021) (see also Section 4.4). Additionally, bandpass selection effects favor the $850 \mu\text{m}$ detection of dusty galaxies at $z \sim 2 - 3$, while sources at both higher and lower redshifts are often missed—particularly at very high redshifts (e.g., near the end of reionization), where dusty galaxies are intrinsically rare. A thorough resolution of these selection effects would require comprehensive multiwavelength surveys of dusty galaxies—well beyond the scope of this work. Readers should simply be aware of these potential biases when evaluating our conclusions.

Based on previous definition, the fraction of SMGs classified as starbursts ranges from $\sim 20\%$ to 40% across different redshifts. On average, $\sim 26\%$ of SMGs are starbursts, in excellent agreement with results for ALESS SMGs ($\sim 27\%$; Cunha et al. 2015), and slightly lower than findings for SCUBA-2 sources in the NEP deep field (Shim et al. 2022).

Our sample further suggests a trend where the fraction of starburst systems increases with $850 \mu\text{m}$ flux and infrared luminosity (the right plot of Figure 5). Barrufet et al. (2020) studied a sample of high-redshift submillimeter-bright galaxies and Herschel color-selected galaxies, which are biased toward brighter submillimeter and infrared sources. Their results show a higher starburst fraction—approximately 40% at $z = 2 - 3$, nearly double our measurement—and they report that Herschel color-selected galaxies exhibit higher starburst fractions than SCUBA-2-selected galaxies.

Approximately 28% of SMGs fall into the quiescent category, a fraction comparable to that of starbursts. Meanwhile, about half ($\sim 46\%$) reside within the star-forming main sequence. The relative fractions of these populations are illustrated in the middle panel of Figure 5. We find that at higher redshifts ($z > 3.5$), starburst systems constitute about half of the sample, dominating the early evolution of SMGs. As redshift decreases, the intense star formation in these systems subsides between $z \sim 2.5 - 3.5$, and most SMGs transition into the stable main sequence phase—a period coinciding with the peak of $850 \mu\text{m}$ -selected SMG observations. During this phase, the starburst fraction drops to $\sim 20\%$, while the main sequence fraction rapidly increases to $\sim 70\%$. Subsequently, at $z \sim 2.5$, the main sequence fraction declines to the average level, while the quenched fraction rises sharply to $\sim 35 - 40\%$. This epoch aligns with the predicted decline in baryon conversion efficiency within massive dark matter halos (and massive galaxies), suggesting that SMG evolution follows

a pathway consistent with galaxies undergoing reduced cold gas accretion (Behroozi et al. 2013). Approximately 1–2 Gyr later, at $z \sim 1.5$, there is a secondary increase in the starburst fraction by about 30% . However, this burst of activity quickly subsides at $z < 1$, with systems transitioning back to the main sequence.

4.1.2. Specific Star Formation Rate

The specific star formation rate ($\text{sSFR} \equiv \text{SFR}/M_{\text{star}}$) quantifies the star formation activity per unit stellar mass in a galaxy (Guzman et al. 1997), reflecting the rate at which the stellar mass fraction grows (Madau & Dickinson 2014), and is commonly used to compare the intensity of star formation across different galaxy populations.

We divide the SMG sample into three stellar mass bins: high-mass ($M_{\text{star}} = 10^{11.4-12} M_{\odot}$), intermediate-mass ($M_{\text{star}} = 10^{10.9-11.4} M_{\odot}$), and low-mass ($M_{\text{star}} = 10^{10-10.9} M_{\odot}$). These bins include 90% of the total sample, with comparable numbers of galaxies in each group. In Figure 6 left image, we plot the evolution of sSFR with redshift for the three groups, with shaded regions indicating the main sequence ranges corresponding to the median masses of each bin.

Our analysis reveals the following: (i) The sSFR of SMGs in all mass bins decreases with decreasing redshift. (ii) A clear anti-correlation exists between sSFR and stellar mass, indicating that more massive galaxies completed the bulk of their star formation earlier and now exhibit lower sSFR compared to less massive systems. This trend is consistent with findings in studies of main sequence galaxies (Guzman et al. 1997; Brinchmann & Ellis 2000; Juneau et al. 2005; Firmani & Avila-Reese 2010). (iii) The SSA22 SMG sample clearly exhibits the “downsizing” phenomenon: as the universe evolves to lower redshifts, star formation activity shifts from the most massive galaxies to lower-mass systems.

Taken together, we arrive at the following picture: The epoch at which baryon conversion efficiency declines in massive dark matter halos corresponds to $z \sim 2.5$ (Behroozi et al. 2013). After this epoch, the most massive SMGs begin to quench, followed by intermediate-mass systems. These higher-mass groups gradually move off the main sequence after cosmic noon, reaching a passive evolutionary phase by $z \sim 1.5$. The downsizing phenomenon leads to the quenching of the most massive galaxies (Miller et al. 2015), likely due to the gradual depletion of gas reservoirs (Noeske et al. 2007b). Concurrently, star formation in the universe becomes increasingly dominated by low-mass galaxies. The low-mass SMG group transitions from a starburst phase to

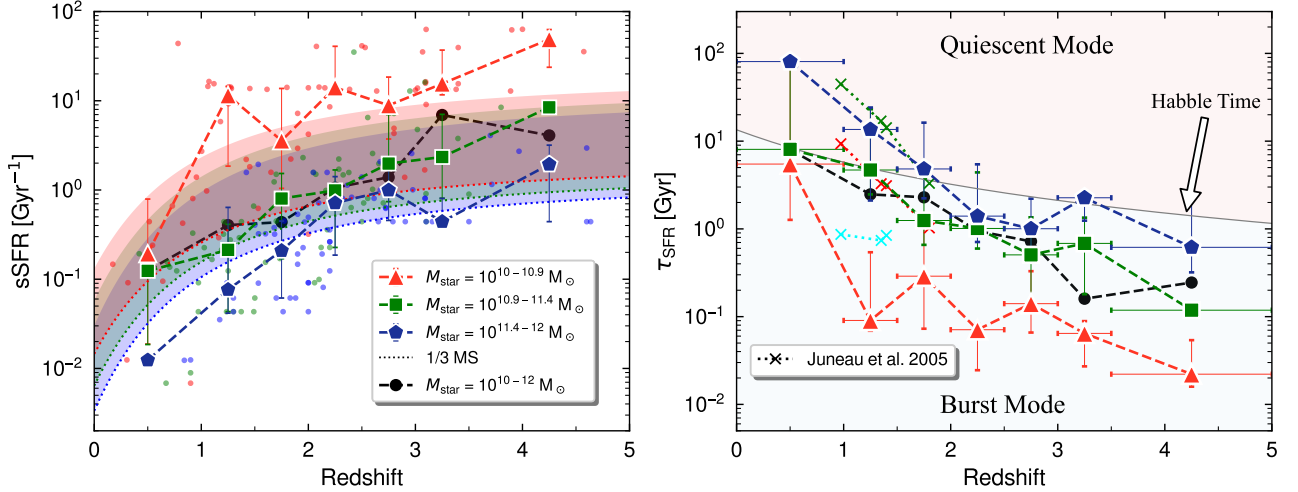


Figure 6. Specific star formation rate ($\text{sSFR} = \text{SFR}/M_{\text{star}}$) and characteristic stellar mass doubling timescale ($\tau_{\text{SFR}} \equiv \rho_{M_{\text{star}}}/\rho_{\text{SFR}}$) for SMGs as a function of redshift, illustrating a clear downsizing trend: more massive galaxies complete their star formation earlier and transition to quiescence, while lower-mass systems dominate the SMG population at later times. Left: sSFR versus redshift. Individual SMGs are shown as small dots, while colored symbols and corresponding shaded regions indicate the median sSFR and main-sequence scatter for different mass bins. Sources below the dotted line are evolving toward quiescence. Right: Characteristic mass-doubling timescale versus redshift. The black curve represents the Hubble time at each redshift; systems above this line exhibit declining star formation activity. The crosses denote the results for optically and near-infrared selected galaxies from Juneau et al. (2005), with green, red, and cyan symbols representing galaxies in stellar mass bins of $10.8 - 11.5$, $10.2 - 10.8$, and $9.0 - 10.2$ (in $\log_{10} M_{\odot}$), respectively.

the main sequence, reaching a stable star-forming state around $z \sim 1$.

The inverse of sSFR corresponds to the characteristic stellar mass doubling timescale (Madau & Dickinson 2014), i.e., the time required to assemble the current stellar mass at the present SFR. Juneau et al. (2005) used the average timescale ($\tau_{\text{SFR}} \equiv \rho_{M_{\text{star}}}/\rho_{\text{SFR}}$) to characterize the transition from burst to quiescent star formation mode across galaxy populations, defining galaxies with τ_{SFR} shorter than the Hubble time as actively star-forming, and those with longer timescales as transitioning into quiescence. As shown in right panel of Figure 6, applying this criterion yields conclusions consistent with our earlier classification, despite the different threshold. Comparing with the results of Juneau et al. (2005), at similar masses, even the reddest galaxies selected in the optical and near-infrared bands quench more rapidly than SMGs. This highlights that at intermediate to low redshifts ($z < 4$), the majority of cosmic star formation occurs obscured by dust (Bourne et al. 2017; Dunlop et al. 2017; Zavala et al. 2021; Bouwens et al. 2022), and particularly at $z \lesssim 2$, dusty star-forming galaxies contribute approximately 80% of the total cosmic star formation activity (Zavala et al. 2021).

4.2. Stellar Mass Assembly History

Using the best-fit SEDs, we reconstruct the stellar formation histories and mass assembly trends over cosmic time for individual galaxies.

Shown in Figure 7, each “spore” represents the assembly history of a single galaxy. We adopt a double-exponential SFH model, which includes a dominant, extended star formation episode and a more recent burst of star formation (Boquien et al. 2019). Although the adopted SFH templates are highly simplified and likely differ from true galactic evolution, current observational techniques cannot recover exact star formation histories. Thus, these abstract models inferred from SED fitting remain valuable for studying galaxy evolution.

The median mass-weighted age Age_m of the sample is 567 Myr (Table 1). When SMGs are categorized by evolutionary stage into main-sequence, starburst, and quiescent subsamples (Section 4.1), the median ages differ significantly, measuring 535 Myr, 374 Myr, and 1900 Myr, respectively. We find that more massive galaxies ($M_{\text{star}} [M_{\odot}] > 10.9$) are predominantly located on the main sequence or are quiescent systems.

Furthermore, following the approach of Merlin et al. (2025), we classify the galaxies into “fast-evolving” and “slow-evolving” types based on whether their Age_m is greater than median mass-weighted age ~ 570 Myr. The majority of quiescent SMGs ($\sim 80\%$) have experienced prolonged evolutionary histories, averaging ~ 2 Gyr. These systems typically formed at $z \gtrsim 3-6$ and

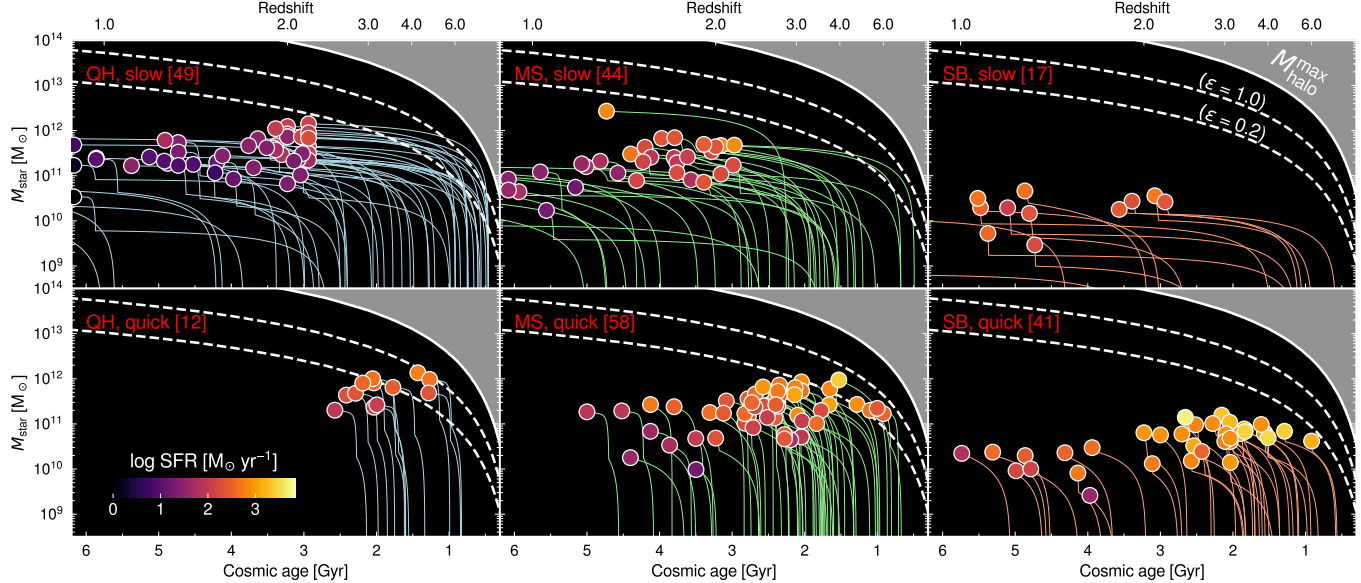


Figure 7. A visualisation of the stellar mass assembly history for each SMG, based on the best-fit star formation history from CIGALE. The red text in the upper-left corner of each subplot indicates whether the galaxy is in a quiescent phase (QH), main sequence (MS), or starburst phase (SB), as well as whether its evolutionary history is slower or faster than the median mass-weighted age ~ 570 Myr. The number of SMGs in each group is given in brackets. The grey shaded area represents the maximum dark matter halo mass allowed within the current survey volume. The dashed lines indicate the efficiency of converting baryonic matter into stars at 20% and 100%, assuming a baryonic fraction of 0.16 in halos.

are observed around $z \sim 2$. Most do not undergo significant secondary star formation episodes, maintaining low SFRs over extended periods. Galaxies that quench at lower redshifts show progressively less active star formation. In contrast, “fast-evolving” quiescent SMGs have generally undergone two intense, closely spaced starbursts, typically forming at $z \sim 3\text{--}4$ with a median age of only 0.4 Gyr. Notably, the second burst in these systems contributes at least an order of magnitude increase in stellar mass.

Main-sequence SMGs are nearly evenly distributed between “fast- and slow-evolving” subpopulations. “Fast-evolving” main-sequence galaxies have ages comparable to quiescent systems (around 0.4 Gyr), but their second star formation episode is less extreme in terms of mass contribution.

Starburst SMGs are generally lower in mass. Their evolutionary tracks show rapid “upward growth”, contrasting with the more massive quiescent galaxies. The median age of starburst SMGs is ~ 260 Myr. Regardless of overall evolutionary speed, starburst galaxies generally undergo or are currently experiencing a second star formation episode, which contributes significantly to their mass assembly—particularly in systems with longer SFHs. This observation is consistent with the view proposed by Merlin et al. (2025) that low-mass galaxies do not remain passively evolving after quenching but may reignite star formation.

Following the method of Xiao et al. (2024), we place simple constraints on the maximum galaxy mass $M_{\text{gal}}^{\text{max}} = \epsilon f_b M_{\text{halo}}^{\text{max}}$ within the survey volume in a Λ CDM framework. Here, ϵ is the baryon-to-star conversion efficiency, f_b is the cosmic baryon fraction, and $M_{\text{halo}}^{\text{max}}$ is the maximum dark matter halo mass. The survey coverage ($\sim 0.27\text{deg}^2$; Section 2) corresponds to a comoving volume of $V \sim 1.5 \times 10^7 \text{ cMpc}^3$, assuming a conservative redshift range of 0–6. Using the Python package `hmf` (Murray et al. 2013), we compute the cumulative halo mass function $n(M_{\text{halo}}^{\text{max}}, z)$. The maximum detectable halo mass at a given time satisfies $n(M_{\text{halo}}^{\text{max}}, z) \times V = 1$. Using the cosmic baryon density Ω_b and matter density Ω_m , we adopt a baryon fraction $f_b = \Omega_b/\Omega_m \simeq 0.16$ (Aghanim et al. 2020), assumed to be constant. We adopt $\epsilon = 0.2$ as the upper limit following common practice (Wechsler & Tinker 2018), even though that studies suggest the conversion efficiencies range of 20–40% (Behroozi et al. 2019; Girelli et al. 2020; Shuntov et al. 2022).

We find that some massive galaxies underwent extremely rapid mass assembly accompanied by high star formation efficiencies (at least $\sim 0.2\text{--}0.8$) at high redshift. These systems typically have $M_{\text{star}} \gtrsim 10^{11\text{--}12} M_{\odot}$ and $\text{SFR} \gtrsim 200\text{--}600 M_{\odot} \text{ yr}^{-1}$, even including those classified as quiescent. They are predominantly lie at high redshifts ($z \gtrsim 4$, i.e., within the first ~ 1.5 Gyr of cosmic time). As noted by Merlin et al. (2025), many

galaxies experienced intense bursts of star formation and rapid quenching within the first billion years, with such rare objects contributing significantly to the cosmic SFR density (Xiao et al. 2024).

While the inferred efficiencies do not exceed 100%, such high values remain puzzling. They may stem from overestimated masses or redshifts in SED fitting, or from oversimplified SFH parameterizations, which may vary substantially with environment and mass. Alternatively, it may reflect simplistic assumptions about universal invariants—such as applying a local IMF to high-redshift galaxies, or assuming a constant baryon fraction across halo masses and redshifts (even though f_b depends on both; Girelli et al. 2020)—among other factors.

However, high-precision spectroscopic redshifts and hydrodynamical simulations confirm the existence of such systems and rule out cosmic variance (Xiao et al. 2024; Merlin et al. 2025). These studies also indicate that star formation in the early universe was significantly more efficient—by factors of 2–3—than at later times (Xiao et al. 2024; Wang et al. 2025). Dekel et al. (2023) proposed a feedback-free starbursts (FBBs) model, suggesting that high gas densities and low metallicities in massive halos at $z \sim 10$ enable highly efficient star formation. Key factors include short free-fall timescales (< 1 Myr) in molecular clouds and efficient gas cooling and accretion via cold streams in a halo, which avoid feedback from massive stars (e.g., winds or supernovae), while dense gas shields subsequent star formation from early generations. Theoretically, such galaxies are predicted to be compact with episodic SFHs (Dekel et al. 2023; Li et al. 2024). As the universe evolves, increasingly extreme halo conditions are required for such efficient bursts, naturally explaining the observed decline in star formation efficiency at lower redshifts.

4.2.1. Age and Lifetime of SMGs

In this section, we investigate the formation and evolutionary timescales of SMGs based on physical properties derived from SED modeling.

We estimate the “mass-weighted age” using the best-fit SFH. Our sample shows a median mass-weighted age of 0.57 ± 0.22 Gyr, with 68% of galaxies lying in the range 0.27–2.10 Gyr, consistent with the average age (0.46 Gyr) of 707 ALMA SMGs in the AS2UDS survey (Dudzevičiūtė et al. 2020).

The mass-weighted ages correlate strongly with star-forming states (Section 4.1): the 102 galaxies on the main sequence have a median age of 0.54 Gyr, while

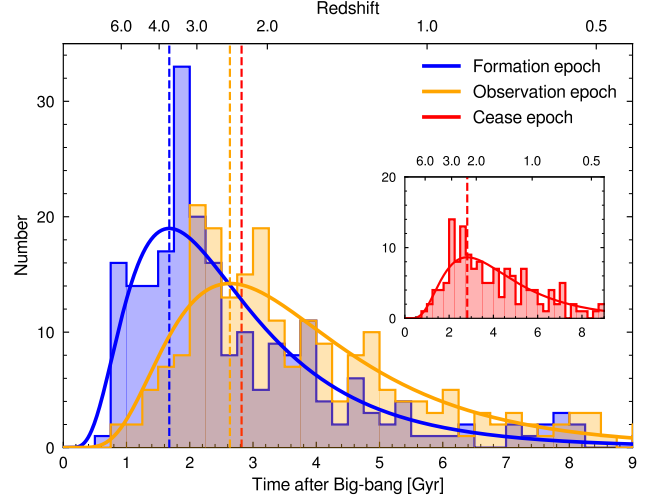


Figure 8. Distribution of SMGs as a function of cosmic age. Using mass-weighted ages and gas depletion timescales, we estimate the formation epoch and the time at which galaxies exit the SMG phase. The solid line shows a logarithmic fit to the distribution, and the dashed line indicates the peak (mode) of the distribution, suggesting that the typical SMG in our sample exits the phase approximately 200 Myr after observation.

the “burst” ($N=58$) and “quenching” phases ($N=61$) systems show 0.37 Gyr and 1.90 Gyr, respectively (Table 1). The average mass-weighted ages of SMGs in the high-mass (66 sources, $10^{11.4-12} M_\odot$), intermediate-mass (65 sources, $10^{10.9-11.4} M_\odot$), and low-mass (66 sources, $10^{10-10.9} M_\odot$) bins are 1.11 Gyr, 0.89 Gyr and 0.49 Gyr, respectively (Table 1).

We define the “characteristic star formation timescale” τ_{sf} as the ratio of stellar mass to current star formation rate, $M_{\text{star}}/\text{SFR}$, with a median value of 1.11 ± 0.2 Gyr, matching AS2UDS results. This timescale varies by over an order of magnitude across different states: 1.06 Gyr for main-sequence, 0.07 Gyr for “burst”, and 10.52 Gyr for “quenching” galaxies.

The gas depletion timescale, $\tau_{\text{dep}} = M_{\text{gas}}/\text{SFR}$, represents the time required to convert the gas reservoir into stars at the present SFR, assuming no replenishment of gas. For simplicity, we adopt the commonly used gas-to-dust ratio $\delta_{\text{gdr}} \sim 100$ (Swinbank et al. 2014; Dudzevičiūtė et al. 2020) to estimate the gas mass as $M_{\text{gas}} = \delta_{\text{gdr}} \times M_{\text{dust}}$. Although this approach is idealized, the gas depletion timescale remains a useful reference for estimating the duration of the SMG phase. The gas depletion timescales of SMGs have median value of ~ 1.31 Gyr in our sample, which is comparable to the τ_{sf} supporting the assumption that, from this perspective, observed SMGs are typically midway through their dusty phase (Dudzevičiūtė et al. 2020). The median de-

Table 1. Average properties of the SSA22 SMGs

Properties	Total sample	QH sample	MS sample	SB sample	HM sample	IM sample	LM sample
	221 SMGs	61 SMGs	102 SMGs	58 SMGs	66 SMGs	65 SMGs	66 SMGs
Age _m [Gyr] ^a	$0.57^{+1.53}_{-0.30}$	$1.90^{+0.23}_{-1.49}$	$0.54^{+1.33}_{-0.17}$	$0.37^{+1.08}_{-0.20}$	$1.11^{+0.99}_{-0.69}$	$0.89^{+1.21}_{-0.60}$	$0.49^{+1.28}_{-0.26}$
$M_{\text{star}}/\text{SFR}$ [Gyr] ^b	$1.11^{+6.95}_{-1.04}$	$10.52^{+12.59}_{-8.26}$	$1.06^{+2.06}_{-0.61}$	$0.07^{+0.04}_{-0.05}$	$2.26^{+9.57}_{-1.60}$	$2.23^{+7.35}_{-1.77}$	$0.09^{+2.23}_{-0.05}$
$100 \times M_{\text{dust}}/\text{SFR}$ [Gyr] ^c	$1.31^{+16.72}_{-1.18}$	$6.68^{+27.35}_{-6.08}$	$0.97^{+12.00}_{-0.77}$	$0.23^{+10.40}_{-0.17}$	$0.98^{+5.96}_{-0.84}$	$1.31^{+18.23}_{-1.13}$	$0.52^{+15.91}_{-0.45}$
sSFR [Gyr ⁻¹]	$0.90^{+12.94}_{-0.77}$	$0.10^{+0.35}_{-0.05}$	$0.94^{+1.25}_{-0.62}$	$14.34^{+29.24}_{-5.23}$	$0.44^{+1.06}_{-0.36}$	$0.45^{+1.76}_{-0.34}$	$11.05^{+16.70}_{-10.62}$
ΔMS ^d	$-0.16^{+0.98}_{-0.61}$	$-0.88^{+0.29}_{-0.33}$	$-0.15^{+0.33}_{-0.20}$	$0.94^{+0.33}_{-0.27}$	$-0.38^{+0.43}_{-0.60}$	$-0.34^{+0.50}_{-0.52}$	$0.67^{+0.46}_{-0.83}$

NOTE—These denote, respectively, the full SMG sample; subsamples classified as quenched, main-sequence, and starburst galaxies; and SMGs divided into higher-, intermediate-, and lower-mass groups.

^aThe mass-weighted ages of the galaxies are derived from CIGALE.

^bCharacteristic star formation timescale (τ_{sf}) as the ratio of stellar mass to current star formation rate, $M_{\text{star}}/\text{SFR}$. See Section 4.2.1

^cCharacteristic gas depletion timescale, $\tau_{\text{dep}} = M_{\text{gas}}/\text{SFR} = \delta_{\text{gdr}} \times M_{\text{dust}}$, we adopt the commonly used gas-to-dust ratio $\delta_{\text{gdr}} \sim 100$ (Section 4.2.1).

^dThe offset of SMGs from the main sequence, defined as $\Delta\text{MS} = \log_{10}(\text{SFR}/\text{SFR}_{\text{MS}})$, where the main sequence relation is adopted from Speagle et al. (2014).

pletion timescales for galaxies on the main sequence and in the “burst” and “quench” phases are 0.97 Gyr, 0.23 Gyr, and 6.68 Gyr, respectively. It should be noted that these timescales assume idealized conditions. In reality, galaxies may accrete additional gas, and existing gas may not be fully consumed due to feedback-driven outflows or sudden quenching of star formation. Furthermore, the SFR can vary significantly over time, including episodes of starbursts or gradual decline.

Using mass-weighted ages as SMG ages and τ_{dep} for remaining duration, we reconstruct evolutionary timelines. Figure 8 shows the distributions of observation times, inferred onset times, and predicted end times of the SMG phase across cosmic history. A simple median analysis suggests that the “formation epoch” of the sample galaxies, the period when they were observed in the SMG phase, and the end of their gas depletion phase are approximately 2.21 Gyr, 3.23 Gyr, and 4.65 Gyr after the Big Bang ($z \sim 2.88, 2.00, 1.33$), respectively. However, the distribution exhibits a long tail and significant scatter in age space, leading to a notable difference between the median and the mode of the distribution. The peak of the observed epoch distribution occurs at an earlier time.

To better characterize the typical evolutionary path, we fit the distributions with log-normal functions and analyze the mode, $\exp(\mu - \sigma^2)$, which represents the most probable value. Here, μ and σ denote the mean and standard deviation of the lognormal distribution,

with the median of the log-normal distribution given by $\exp(\mu)$. The peak of the observed epoch distribution is at 2.63 Gyr (corresponding to $z \sim 2.44$), with fitted parameters $\mu = 1.23 \pm 0.03$ and $\sigma = 0.52 \pm 0.02$. These massive galaxies began to form extensively around 1.68 Gyr ($z \sim 3.67$), with $\mu = 0.86 \pm 0.04$ and $\sigma = 0.58 \pm 0.03$. The end of the phase peaks at 2.82 Gyr ($z \sim 2.29$), with $\mu = 1.97 \pm 0.08$ and $\sigma = 1.23 \pm 0.06$.

From this perspective, the majority of galaxies in our sample started forming around 1.68 Gyr after the Big Bang. Approximately 1 Gyr later, they entered the ‘SMG phase’ and were observed. After an additional ~ 0.2 Gyr, these galaxies largely transitioned out of the ‘SMG phase’, becoming quiescent and redder.

4.3. The Contribution of SMGs

4.3.1. Contribution to the SFRD

To quantify the contribution of SSA22 deep field SMGs to the cosmic SFRD, we first sum the SFRs of all galaxies within each redshift bin. These values are then corrected for completeness and false detection rates, and divided by the comoving volume corresponding to the survey area and redshift range (i.e., the difference in comoving volumes between the upper and lower redshift boundaries). Given that the deepest 850 μm observations ($\sigma_{850} \pm 1 \text{ mJy beam}^{-1}$) in the central region provide the most complete multi-wavelength coverage, all statistical results discussed in this section are derived from this area. The uncertainties in SFRD estimates are

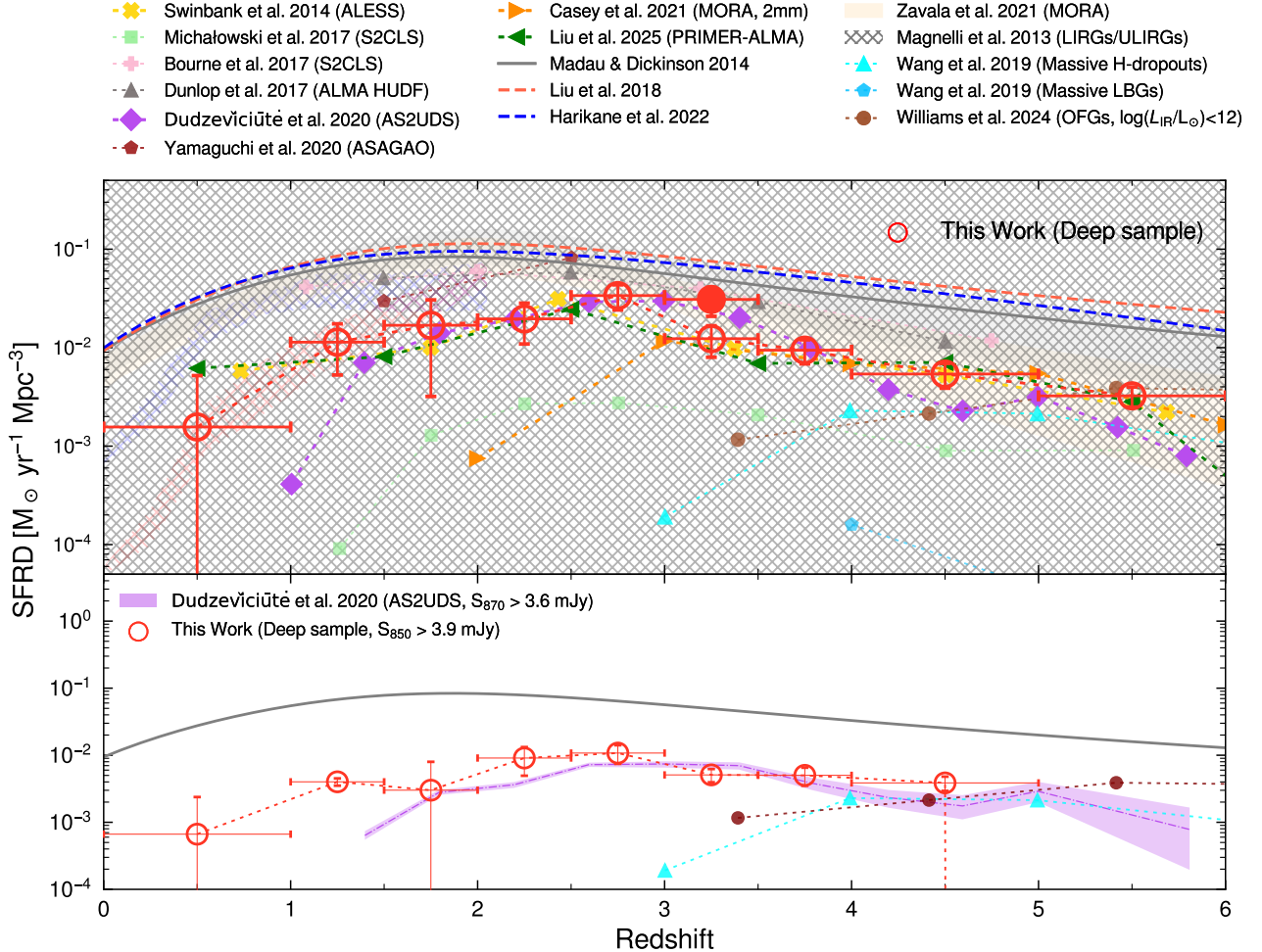


Figure 9. Top: Contribution of SSA22 SMGs to the cosmic star formation rate density, with a sample-averaged fraction of 23%. Our results align with those from other large surveys, peaking within the redshift range of 2.5–3. Red filled circles include SMGs in the $z = 3.09 (\pm 0.05)$ overdense region, highlighting the significant contribution from dense environments. The red and blue grids represent the contributions from ULIRGs and LIRGs (Magnelli et al. 2013), respectively, while the yellow and gray shaded regions indicate the dust-obscured star formation activity and the total SFRD inferred by Zavala et al. (2021). Bottom: Contribution of brighter SMGs, consistent with results from AS2UDS bright SMGs and H-dropouts.

based on Poisson statistics. For consistent comparison with literature values, we apply the following conversions to SFR and stellar mass measurements originally based on different IMFs. Specifically, SFRs and stellar masses derived using a Salpeter (1955) IMF are multiplied by 0.63 and 0.61, respectively, while those based on a Kroupa & Weidner (2003) IMF are scaled by 0.94 and 0.92, respectively (Madau & Dickinson 2014; Lim et al. 2020a).

In addition to the results from Madau & Dickinson (2014), we have included SFRD estimates from Liu et al. (2018) and Harikane et al. (2022) in our figures. It is important to note that at high redshifts ($z > 4$), the SFRD curve from Madau & Dickinson (2014) is constrained by only two UV surveys. Recent dropout surveys and higher-redshift JWST observations support slightly ele-

vated SFRD values (Harikane et al. 2022, 2025). Liu et al. (2018) combined direct FIR+mm observations with those from Madau & Dickinson (2014), resulting in a total SFRD estimate that is approximately 1.5 to 1.7 times higher than that of Madau & Dickinson (2014). For consistency in previous literature and subsequent discussions, we reference the SFRD values from Madau & Dickinson (2014); however, it should be noted that these values represent upper limits when compared to more recent findings.

On average, the SMG contribution in the SSA22 deep field is approximately 21%. As shown in Figure 9, our results closely match those of Swinbank et al. (2014); Dudzevičiūtė et al. (2020); Casey et al. (2021); Liu et al. (2025), demonstrating that counterpart identification and advanced deblending techniques successfully resolve

highly confused SCUBA-2 sources into individual SMGs, pushing the $850 \mu\text{m}$ detection limit to $\sim 1 \text{ mJy}$.

By cosmic noon ($z \sim 2$), SMGs contribute only $\sim 20\%$ of the cosmic star formation, decreasing to $< 5\%$ at $z < 1$. Magnelli et al. (2013) also found that $z \lesssim 1.5$, the cosmic SFRD becomes dominated by luminous infrared galaxies (LIRGs), while at later epochs it is increasingly driven by fainter sources (i.e., sub-LIRGs). This universal trend illustrates the “downsizing” scenario: infrared-bright massive galaxies gradually quench their extreme star formation, transitioning out of the SMG phase into passive evolution (Miller et al. 2015), while lower-mass galaxies dominate star formation.

From another perspective, our sample at $z < 1$ mainly consists of LIRGs, and at $z = 1\text{-}2$, includes ULIRGs. However, their contribution is only comparable to *Herschel*-selected ULIRGs (Magnelli et al. 2013), and significantly lower than the total SFRD. Several studies on the dust temperature and luminosity of SMGs provide useful insights: $850 \mu\text{m}$ -selected SMGs tend to be cooler than *Herschel*-selected sources (Simpson et al. 2017; Dudzevičiūtė et al. 2020; Liao et al. 2024) and exhibit lower average temperatures compared to local and low- z samples (Dudzevičiūtė et al. 2020). At fixed luminosity, cooler SMGs show higher submillimeter fluxes (Swinbank et al. 2014; Cunha et al. 2015). This suggests that at $z \lesssim 1\text{-}2$, current surveys miss numerous $850 \mu\text{m}$ -faint but hotter galaxies, highlighting the limitations of $850 \mu\text{m}$ observations for detecting warm infrared sources at these redshifts and the need for shorter-wavelength surveys.

In the redshift range $z = 2\text{-}2.5$, the ASAGAO survey combined with archival data achieves a 1σ depth of $0.1\text{-}0.2 \text{ mJy}$ at $850 \mu\text{m}$ (assuming a dust emissivity index $\beta=1.8$), corresponding to $L_{\text{IR}} \sim 10^{11} L_{\odot}$ and resolving most of the cosmic infrared SFRD. The SSA22 deep field contributes about 25% of this SFRD, approximately 1/3 to 1/4 of the ASAGAO results (Yamaguchi et al. 2020).

At $z = 2.5\text{-}3.5$, the SSA22 SMGs account for 50-60% of the SFRD relative to Madau & Dickinson (2014). For $z = 3\text{-}3.5$, ALMA HDUF and S2CLS $850 \mu\text{m}$ archival data (Bourne et al. 2017; Dunlop et al. 2017) reach a depth of $\sim 0.2 \text{ mJy}$ (assuming $\beta=1.8$), revealing that faint submillimeter galaxies contribute significantly to cosmic star formation (Michałowski et al. 2017). Including the overdense region at $z = 3.09$ (solid red dot in the figure), our sample contributes $\sim 62\%$ of the cosmic SFRD, consistent with these surveys. However, if we exclude the contribution from the overdense regions (open circles, removing sources within the 3.09 ± 0.05 range), SMGs then account for approximately 25% of the SFRD, consistent with the fraction observed at $z =$

2-2.5. This indicates that overdense environments or large-scale structures significantly enhance the contribution to the infrared background.

As shown in the Figure 9, the majority of the SMG sample reaches its peak contribution to the cosmic SFRD at $z \sim 2.5\text{-}3$, approximately 1.5 Gyr earlier than the “cosmic noon”. Both ultra-deep surveys (Bourne et al. 2017; Dunlop et al. 2017) and model (Zavala et al. 2021) suggest that dust-obsured star formation during this period accounts for about 80% of the total SFRD. Dunlop et al. (2017) argue that the dominance of the dusty component in the cosmic SFRD during this epoch is primarily driven by the rapid increase in the number density of massive, dusty star-forming galaxies, with the evolution of galaxy dust fractions playing a secondary role. This also suggests rapid evolution of ULIRGs in the early universe, where massive galaxies quickly accumulate stars and dust, eventually forming today’s most massive elliptical galaxies and cluster members (Wang et al. 2019).

Dunlop et al. (2017); Zavala et al. (2021) further note that at $z > 4$, dusty star-forming galaxies become increasingly rare, marking a transition in cosmic star formation activity from a dust-obsured to an unobsured mode. Their contribution to the cosmic SFRD declines sharply, falling to approximately 25-35% at redshifts $z \sim 5\text{-}6$. The SSA22 $850 \mu\text{m}$ -selected galaxies reflect this trend, with contributions declining rapidly to $\sim 20\text{-}25\%$ of the cosmic SFRD at $z > 3$, consistent with other surveys.

For bright $850 \mu\text{m}$ sources ($S_{850} > 3.9 \text{ mJy}$), we estimate their contribution to the SFRD and compare it with the AS2UDS sample ($S_{870} > 3.6 \text{ mJy}$). As shown in the lower panel of Figure 9, both samples yield consistent SFRD estimates. These bright SMGs still contribute $\sim 10\text{-}20\%$ of the cosmic SFRD at $z = 2\text{-}4$.

At $z \gtrsim 4$, ALMA and far-infrared detections become sparse. Consequently, estimates of the dust-obsured SFRD at high redshifts often rely on a small number of bright sources and extrapolations of the infrared luminosity function (Madau & Dickinson 2014; Liu et al. 2018; Gruppioni et al. 2020). The faint-end shape of the luminosity function in the early universe remains highly uncertain (Traina et al. 2024). Studying dust-obsured star formation during this epoch requires a broader suite of observational approaches.

Wang et al. (2019) identified a population of H-dropouts at $z \sim 4\text{-}6$, which exhibit faint (sub)millimeter fluxes and are predominantly massive, dusty star-forming galaxies. Their contribution to the cosmic SFRD is comparable to that of brighter SMGs at the same epoch and amounts to approximately 10% of the

contribution from Lyman-break galaxies (LBGs). However, when matched in stellar mass, the contribute of massive LBGs (shown as blue triangles in Figure 9) is significantly lower than that of star-forming galaxies or SMGs, by ~ 2 dex. This indicates that in the early universe, star formation in the most massive galaxies was predominantly obscured by dust, and that dusty star-forming galaxies constitute the majority of the massive galaxy population (Wang et al. 2019). This result further demonstrates that at $z > 3$, most of the most massive galaxies are indeed optically faint (Wang et al. 2019).

Recently, analyses have been conducted on JWST-selected optically faint galaxies (OFGs), many of which are H-dropouts or similar optical-faint populations (Williams et al. 2024). The majority of OFGs are extended, high-redshift dusty star-forming systems (Wang et al. 2019; Barrufet et al. 2025), with SFRs range from 10 to 100 $M_{\odot} \text{ yr}^{-1}$ and stellar masses that are 1-2 dex lower than those of typical SMGs (Gottumukkala et al. 2024; Williams et al. 2024). OFGs were often entirely missed by HST and lie below the typical detection limit of ALMA ($\log_{10}(L_{\text{IR}}/L_{\odot}) < 12$) (Williams et al. 2024). At $z \lesssim 4.5$, OFGs account for only a modest portion of the dust-obscured SFRD ($\sim 26\%$; brown circles in figure 9). However, their contribution becomes substantial at $z \gtrsim 5.7$, which comparable to previous estimates derived from extrapolated infrared luminosity functions, although “little red dots” (LRDs) dominate the SFRD at $z > 6$. The growing role of OFGs implies that past infrared/(sub)millimeter surveys may have missed up to half of the obscured star formation at these redshifts. High-redshift OFGs thus offer a promising avenue to place tighter constraints on cosmic SFRD in the post-reionization era (Williams et al. 2024).

4.3.2. Contribution to the SMD

Following the same methodology as described above, we calculate the cosmic SMD contribution of SMGs in the SSA22 deep field by summing the stellar masses of all SMGs within each redshift bin, with Poisson errors.

Our results are compared with three major recent surveys (three colorful bands in Figure 10): the $\sim 10 \text{ deg}^2$ Cosmic Dawn Survey Pre-launch by the Euclid telescope (Euclid Collaboration et al. 2025), the $\sim 0.5 \text{ deg}^2$ JWST COSMOS-Web survey (Shuntov et al. 2025), and the $\sim 1 \text{ deg}^2$ COSMOS2020 project (Weaver et al. 2023). These surveys show discrepancies with Madau & Dickinson (2014), who derived SMD by integrating the observed SFRD with a fixed conversion factor of 44% (for a Chabrier IMF), accounting for stellar mass loss during star formation history. This approach may be affected

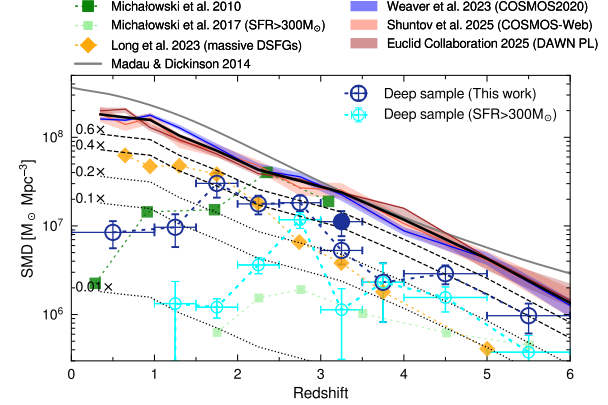


Figure 10. The contribution of SMGs to the cosmic stellar mass density. We compare our results with the average measurements from three major survey programs (Euclid Collaboration et al. 2025; Shuntov et al. 2025; Weaver et al. 2023). The black solid, dashed, and dotted lines represent this averaged reference, with each line corresponding to a specific fractional contribution to the cosmic SFRD or SMD. The contribution levels—ranging from 1% to 60%—are labeled on the left side of the respective lines. By averaging recent large survey data on cosmic SMD, we find that SSA22 SMGs contribute an average of $\sim 28\%$. Blue filled circles include contributions from SMGs within the redshift range of 3.09 ± 0.05 , again emphasizing significant contributions from overdense regions.

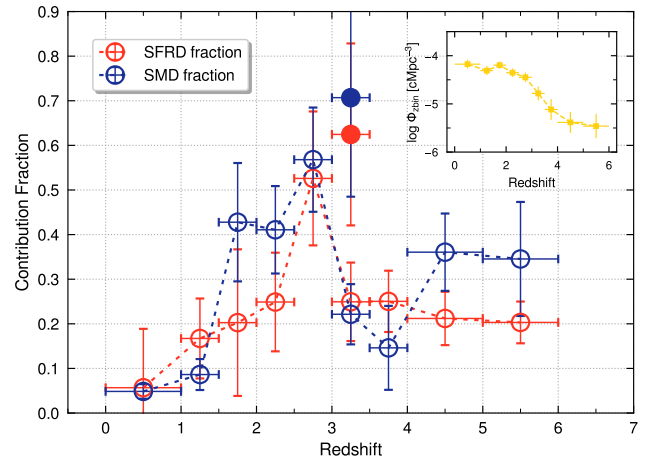


Figure 11. The fractional contribution of SMGs to the universe (solid symbols including overdense regions) as a function of redshift, peaking at 2.5–3 with values exceeding 50%. The inset in the upper right corner shows the number density of SMGs within the survey volume, which increases sixfold below redshift 4, reaching densities of about $2-3 \times 10^{-5} \text{ cMpc}^{-3}$ between redshifts 1–3.

by potential IMF evolution and baryon conversion efficiency, leading to differences between SFRD-derived and directly observed SMD. Furthermore, [Euclid Collaboration et al. \(2025\)](#) attribute the low-redshift discrepancies to improved data quality and uniformity, while the high-redshift differences may reflect a lag between rapid star formation and mass growth ([Weaver et al. 2023](#)). However, it is more likely that these discrepancies are influenced by data and methodology: the high-redshift results of [Madau & Dickinson \(2014\)](#) were based on only two data points. Alternatively, systematic effects such as overestimated dust attenuation, uncertain UV-to-SFR conversion factors, and SED modeling uncertainties could play a role ([Weaver et al. 2023; Shuntov et al. 2025](#)).

On average, SSA22 SMGs contribute approximately 28% to the cosmic SMD (Figure 10). At $z \sim 4$, dust-obscured and unobscured star formation contribute comparably to the cosmic SFRD ([Bourne et al. 2017; Dunlop et al. 2017; Zavala et al. 2021](#)). [Zavala et al. \(2021\)](#) suggested that at higher redshifts ($z = 4\text{--}6$), the scarcity of dust-rich DSFGs results in a significant deficit of infrared emission relative to UV emission, indicating that unobscured star formation dominates cosmic star formation at these epochs. Despite their low number density at high redshift—approximately $3\text{--}4 \times 10^{-6} \text{ cMpc}^{-3}$ at $z \sim 4\text{--}6$ —these rare, massive galaxies contribute $\sim 20\text{--}25\%$ to the cosmic SFRD and $\sim 35\text{--}40\%$ to the SMD (Figure 11).

At later epochs ($z < 4$), dust-obscured star formation rapidly increases, dominating the cosmic SFRD and surpassing the contribution of UV-selected samples. Even among UV-bright galaxies with $M_{\text{star}} > 10^{10} M_{\odot}$, star formation is predominantly obscured ([Bourne et al. 2017](#)).

From the early universe to $z \sim 1\text{--}3$, the comoving number density of SMGs increases by roughly an order of magnitude, reaching $\sim 4\text{--}6 \times 10^{-5} \text{ cMpc}^{-3}$. The SSA22 SMGs reach peak contributions at $z = 2.5\text{--}3.5$, accounting for 50-60% of the cosmic SFRD (including overdense regions) and a similar fraction of the SMD (Figure 11). [Michałowski et al. \(2010\)](#) reported that during this epoch, SMGs account for more than 60% of the SMD, and at $z \sim 2\text{--}2.5$, their survey resolves nearly all of the stellar mass assembled in dusty systems. [Long et al. \(2023\)](#) used numerical models to estimate the contribution of massive DSFGs to the cosmic SMD, finding excellent agreement with observational SMG surveys over the redshift range $z \sim 2\text{--}4$.

The number density of SMGs remains relatively stable between $z = 1.5$ and 2.5 , yet the contribution of SMGs to the cosmic SFRD declines rapidly—becoming compa-

rable to that at $z \sim 4\text{--}6$ (Figure 11). This decline may be attributed to the overall slowdown in cosmic star formation and a reduced efficiency in converting baryons into stars. During this epoch, the contribution of SMGs to the SMD ($\gtrsim 40\%$) exceeds that to the SFRD. This discrepancy may arise from the substantial stellar mass accumulated by SMGs that are gradually quenching. Alternatively, the increased contribution from lower-mass galaxies may be delayed relative to the peak activity of SMGs, similar to the lag observed between cosmic noon and the peak of SMG activity. Uncertainties in the completeness of these large surveys could also contribute to this effect.

[Zavala et al. \(2021\)](#) argued that the contribution of DSFGs to the cosmic SFRD remained relatively constant to the present day after reaching its peak ($\gtrsim 80\%$). Moreover, [Long et al. \(2023\)](#) suggest that the contribution of DSFGs to the SMD shows only mild evolution at $z \lesssim 2$. However, as shown in Figure 10, our SMG sample—consistent with [Michałowski et al. \(2010\)](#)—exhibits a rapid decline at $z < 1.5$, with the contribution of SMGs to both the SFRD and SMD dropping sharply to $\lesssim 10\%$. The contribution from bright SMGs also diminishes quickly after $z \sim 2.5$, becoming negligible by this epoch. This trend is further supported by [McKinney et al. \(2025\)](#), who report a sharp drop in the number density of SMGs, indicating that massive dusty galaxies are increasingly difficult to detect in submillimeter surveys at low redshifts. These observations collectively reflect the quenching of star formation in massive SMGs. Dust-obscured star formation—and the associated buildup of stellar mass—has progressively shifted toward lower-mass dusty systems (i.e., downsizing), whose individual contributions to the cosmic SFRD and SMD are small. Additionally, other populations of dusty galaxies not efficiently traced by $850 \mu\text{m}$ selection—such as warmer, less luminous, or more compact systems—may dominate obscured star formation at late times but remain underrepresented in current submillimeter surveys. (i.e., wavelength selection effects, section 4.4)

4.4. Evolution of SMGs

In the introduction, we provided a brief overview of the formation and evolutionary mechanisms of SMGs. In this section, we describe the evolution of SMGs from a phenomenological perspective, based on statistical observational results, and offer brief interpretive discussions.

Our analysis leads to the following synthesis: In the early universe—around the epoch marking the end of reionization—massive DSFGs are exceedingly rare com-

pared to UV-selected massive galaxies, and the infrared emission associated with dust-obscured star formation is far fainter than the cosmic ultraviolet/optical background. At $z = 5\text{--}6$, the comoving number density of dusty galaxies selected at $850\text{ }\mu\text{m}$ and $\sim 1\text{ mm}$ is approximately $3\text{--}4 \times 10^{-6}\text{ cMpc}^{-3}$ (McKinney et al. 2025) (Figure 11). The contribution from galaxies detected in typical $850\text{ }\mu\text{m}$ surveys accounts for about 20% of the total SFRD at these redshifts (Figure 11), which, relative to the results of Madau & Dickinson (2014), represents an upper limit. Moreover, Zavala et al. (2021) argue that the total dust-obscured star formation activity still contributes $\sim 25\text{--}35\%$ to the SFRD at $z = 5\text{--}6$.

By $z \sim 4\text{--}5$, star formation increasingly occurred within dense, dusty environments, surpassing unobscured modes in contribution (Dunlop et al. 2017). This transition is reflected in the rising dust attenuation observed in both UV- and IR-selected galaxies (Paper III), signaling a global shift from an unobscured to a dust-obscured regime (Zavala et al. 2021). Harikane et al. (2022) suggest that galaxy star formation activity may be regulated by the assembly of dark matter halos. During this epoch, a small subset of the most massive galaxies exhibited exceptionally high baryon conversion efficiencies (Xiao et al. 2024; Merlin et al. 2025) (Figure 7).

SMGs undergo intense star formation primarily at $z \sim 2\text{--}5$ (Thomas et al. 2005), likely fueled by gas-rich major mergers (Engel et al. 2010; Toft et al. 2014; Chen et al. 2015; Hodge et al. 2025). Nevertheless, morphological and simulation studies indicate that the distribution of galaxy morphologies among SMGs resembles that of the general field population (Swinbank et al. 2010; Casey et al. 2014; McAlpine et al. 2019; Gillman et al. 2024), suggesting their evolutionary pathways may not be fundamentally distinct. Indeed, a significant fraction ($\gtrsim 40\text{--}70\%$) of SMGs appear to be driven by secular processes—such as smooth gas accretion and disk instabilities—rather than violent interactions (Magnelli et al. 2012; Gillman et al. 2024; Chan et al. 2025; Zhang et al. 2025). Observations consistently place SMGs at the high-mass end of the star-forming main sequence (Michałowski et al. 2012; Cunha et al. 2015; Dunlop et al. 2017; Lim et al. 2020a).

The comoving number density of these galaxies increases rapidly below redshift ~ 4 (Dunlop et al. 2017; Fujimoto et al. 2024; Traina et al. 2024), rising by roughly an order of magnitude to $\sim 4\text{--}6 \times 10^{-5}\text{ cMpc}^{-3}$ (Figure 11), when (sub)millimeter galaxies become abundantly detectable. This is consistent with the conclusion of Harikane et al. (2022), who attribute the rise in cosmic SFRD from $z \sim 10$ to $z \lesssim 4$ primarily to the rapid increase in the number density of dark mat-

ter halos. By $z \sim 2\text{--}3$, massive DSFGs reach their peak activity. The median redshift of $850\text{ }\mu\text{m}$ -selected SMGs lies in the range $2.3\text{--}2.7$, and the mode of the redshift distribution in our sample is approximately 2.44. During this epoch, SMGs dominate cosmic star formation, contributing $\sim 50\text{--}60\%$ to the SFRD—a fraction that depends on survey depth. Moreover, Zavala et al. (2021) estimate that dust-obscured star formation as a whole accounts for $\sim 80\%$ of the total SFRD at this cosmic peak.

This peak activity is short-lived. Due to their extreme star formation rates, SMGs have gas depletion timescales of only tens to a few hundred Myr (Toft et al. 2014). Noeske et al. (2007a) argue that the global decline in the cosmic SFRD is primarily driven by the progressive exhaustion of gas reservoirs in galaxies. In our sample, the modal gas consumption timescale is ~ 200 Myr (Section 4.2.1, Figure 8). Environmental effects further accelerate quenching in overdense regions (Peng et al. 2010). Concurrently, below $z \sim 2\text{--}2.5$, the baryon conversion efficiency within the massive dark matter halos hosting SMGs ($M_{\text{halo}} \gtrsim 10^{13}\text{ }h^{-1}\text{ }M_{\odot}$) drops precipitously (Behroozi et al. 2013). This decline is consistent with the “cold-mode” gas accretion model (Birnboim & Dekel 2003): at $z \lesssim 2$, inflowing gas in massive halos is typically shock-heated to the virial temperature (Dekel & Birnboim 2006), effectively cutting off the supply of cold gas and quenching further star formation. Consequently, many massive SMGs ($M_* \sim 10^{11}\text{ }M_{\odot}$) begin transitioning to quiescence during this epoch (Figure 5, Figure 6), leading to a declining contribution to both the cosmic SFRD and stellar mass assembly.

At $z \sim 1.5\text{--}2.5$, although the number density of $850\text{ }\mu\text{m}$ SMGs remains roughly constant, their contribution to both the cosmic SFRD and SMD declines rapidly, reaching approximately 20% and 40%, respectively—levels comparable to those at $z = 4\text{--}6$ (Figure 11). The results from Harikane et al. (2022) further indicate that from $z \sim 2$ to $z \sim 0$, cosmic expansion leads to a sharp decline in the halo accretion rate. Consequently, despite a modest increase in the star formation efficiency, the overall cosmic SFRD exhibits a declining trend.

In contrast, lower-mass galaxies ignite their main star formation episodes later Noeske et al. (2007b). At $z > 2$, they exhibit lower metallicities (Cowie et al. 1996; Nelan et al. 2005; Thomas et al. 2005; Pilyugin & Thuan 2011) and higher sSFR. Their star formation declines more gradually (Noeske et al. 2007b), partly because stellar feedback in shallower potential wells prolongs gas retention and star formation (Neistein et al. 2006). Thus, by $z \lesssim 1.5\text{--}2.5$, as massive galaxies transition from bursty

to quiescent modes under the influence of “downsizing”, the locus of cosmic star formation shifts toward lower-mass systems (Cowie et al. 1996; Brinchmann & Ellis 2000; Juneau et al. 2005), which sustain elevated sSFR over longer timescales (Noeske et al. 2007b).

At $z \sim 1$ –1.5, the contribution of SMGs declines rapidly, accompanied by a decrease in their number density (McKinney et al. 2025). By $z < 1$, 850 μm and millimeter-wave surveys struggle to detect SMGs altogether.

In addition to the aforementioned mechanisms of “mass quenching”, “environmental quenching”, and “halo quenching”, AGN feedback also plays a non-negligible role in quenching star formation in massive galaxies. Low-luminosity AGN are commonly detected in massive quiescent galaxies at $z \sim 2$ (Olsen et al. 2013), suggesting active involvement in quenching. Merlin et al. (2025) report strong broad emission lines indicative of AGN activity in \sim 1/3 of their massive quiescent sample. Stellar feedback, too, can act in concert: intense starbursts may heat and expel gas from even deep potential wells on Myr timescales (Merlin et al. 2012). Given that most observed SMGs are dominated by disk structures, morphological quenching (also known as Q-quenching) may occur if the growth of a central bulge stabilizes the disk, thereby suppressing gas fragmentation and star formation (Martig et al. 2009). Furthermore, rapid mass acquisition can also quench galaxy star formation. Oser et al. (2010) showed that in cosmological simulations, stellar mass assembly appears to occur in “two-phase”: early in situ star formation via cold accretion, followed by later structural growth through minor mergers that increase size and mass without reigniting star formation, thereby accelerating quenching.

Brinchmann & Ellis (2000) note that fewer than 10% of local massive ellipticals formed via recent ($z < 1$) major mergers, implying most originated from high-redshift interacting systems. In the context of SMGs, one view holds that massive galaxies gradually evolve into compact quiescent systems at $z \sim 1$ –2 (Barro et al. 2013; Dekel & Burkert 2013; Chen et al. 2015), and later into ellipticals via dry mergers (Toft et al. 2014). However, observations complicate this picture. Recent studies reveal that the majority of SMGs are disk-dominated (Gillman et al. 2023, 2024; Le Bail et al. 2024; Chan et al. 2025; Hodge et al. 2025; Zhang et al. 2025). Concurrently, Gillman et al. (2024) demonstrate that the stellar disk structures of SMGs can persist down to $z \sim 1$. Theoretical work also indicates that disk rebuilding after a merger is feasible through mechanisms such as environmental gas accretion or other processes (Governato

et al. 2009; Barro et al. 2013). Do massive DSFGs primarily evolve into local elliptical galaxies through a sequence of compaction (e.g., major mergers, violent disk instability) followed by slow expansion via minor mergers? Or do a significant fraction evolve directly into massive late-type galaxies in the local universe? Alternatively, is the evolutionary landscape more complex, with multiple pathways coexisting rather than a single dominant channel? Resolving the evolutionary trajectories of massive galaxies is essential for understanding the present-day universe.

Finally, we discuss the “downsizing” phenomenon and the scarcity of SMGs detected at $z \lesssim 1$ in submillimeter surveys. A robust observational trend in galaxy evolution is “downsizing”: massive galaxies complete their star formation early (at high redshift), while lower-mass systems remain actively forming stars to lower redshifts. First articulated by Cowie et al. (1996) to explain low metallicities in high- z damped Lyman- α systems, this paradigm has been reinforced by numerous studies. Brinchmann & Ellis (2000) showed that most massive galaxies had already quenched by $z \sim 1$, whereas low-mass galaxies continued forming stars. Environmental dependence was highlighted by Thomas et al. (2005), who found earlier quenching in denser regions. Nelan et al. (2005) and Pilyugin & Thuan (2011) observed a “downsizing” trend in metallicity as a function of galaxy mass. Using a galactic hybrid evolutionary tracks model, Firmani & Avila-Reese (2010) successfully reproduced the “downsizing” signature reflected in the stellar mass–halo mass relation at various redshifts. Overall, the downsizing phenomenon appears to be a general pattern in galaxy evolution, manifested in both early- and late-type galaxies, as well as in the red and blue sequences. Why is downsizing so pervasive? It reflects two intertwined processes: (1) rapid, early star formation and quenching in massive systems, and (2) prolonged, lower-level activity in low-mass galaxies that dominates the SFRD at late times. Noeske et al. (2007b) framed this as “staged galaxy formation”: low-mass galaxies start forming stars later and exhibit longer e-folding times for SFR decline, resulting in higher sSFR at low z . Massive galaxies, by contrast, experience early, intense bursts—potentially triggered by internal instabilities (Gillman et al. 2024) or enhanced merger rates in dense environments (Thomas et al. 2005)—and assemble their stars rapidly (Neistein et al. 2006), exhausting their gas reservoirs early.

Observationally, SMGs become increasingly elusive at $z \lesssim 1$. As shown in Section 4.3.1, their contribution to the SFRD drops sharply below $z \sim 1.5$, with LIRGs taking over, and sub-LIRGs dominating at even later

times (Magnelli et al. 2013). We attribute this decline to three primary factors: First, quenching and gas exhaustion. In the massive halos ($M_{\text{halo}} \gtrsim 10^{13} h^{-1} M_{\odot}$) typical of SMGs, baryon conversion efficiency plummets below $z \sim 2.5$, with star formation efficiency (SFE) falling from $\sim 10\%$ to just a few percent (Behroozi et al. 2013; Shuntov et al. 2022). Coupled with short gas depletion times (\lesssim few hundred Myr), most SMGs quench before $z \sim 1.5$. Moreover, the cosmic molecular gas density peaks at $z \sim 1.5\text{--}2$ and declines thereafter, with gas fractions dropping and depletion times increasing rapidly (Liu et al. 2019). Second, the downsizing effect itself: the most extreme, IR-luminous starbursts in massive galaxies fade, leaving lower-mass systems to dominate ongoing star formation (Miller et al. 2015). Third, selection effects due to wavelength and dust temperature. At fixed infrared luminosity, colder dust produces a peak that shifts to longer wavelengths and consequently yields a higher observed 850 μm flux (Swinbank et al. 2014; Cunha et al. 2015). Thus, 850 μm surveys preferentially select colder, high-redshift SMGs (Simpson et al. 2017; Dudzevičiūtė et al. 2020; Liao et al. 2024), while missing warmer, low-redshift analogs (see Figure 2 panel a). Indeed, local ULIRGs typically exhibit warmer dust temperatures than high- z SMGs (Symeonidis et al. 2013; Clements et al. 2018), and Chen et al. (2021) demonstrated that submillimeter surveys systematically miss galaxies with hotter dust. This is reflected in the statistics: as redshift decreases, the maximum infrared luminosity of galaxies detected at 850 μm also declines (see Paper III). Consequently, at $z \lesssim 1\text{--}1.5$, current 850 μm surveys likely miss a substantial population of dust-obscured star formers that are faint in the submillimeter but bright in shorter-wavelength IR bands. This is consistent with the well-established trend that longer-wavelength selections probe higher-redshift populations (Casey et al. 2014; Zavala et al. 2014; Wang et al. 2017), while shorter wavelengths trace lower-redshift obscured activity (Magnelli et al. 2013).

5. IR-RADIO CORRELATION

In this section, we present the relationship between radio and submillimeter emission for our SMG sample and characterize the distribution of the quantitative parameter q_{IR} (Section 5.1). The IRRC is remarkably robust; as briefly reviewed in Section 1, it appears to hold out to high redshifts. However, whether the IRRC—or equivalently, the q_{IR} parameter—undergoes cosmic evolution remains debated. We address this question using our data and offer a brief discussion (Section 5.1.1). Finally, we examine the ratio of submillimeter to radio flux densities (Section 5.2).

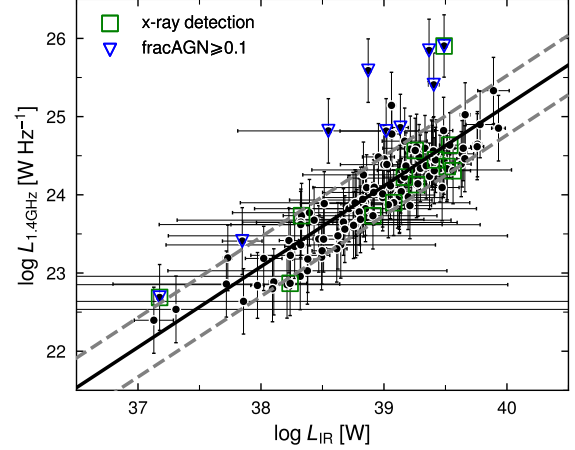


Figure 12. The tight correlation between radio luminosity and infrared luminosity of SMGs in the SSA22 field, both of which directly trace star formation activity within these galaxies. The black solid line represents the linear regression fit, with gray dashed lines delineating the 1σ scatter of 0.38 dex. The open green squares represent sources detected in X-rays, while the open blue triangles indicate galaxies with an AGN fraction greater than 0.1 as inferred from SED fitting. Galaxies with higher AGN fractions deviate due to excess radio emission. Most X-ray detected SMGs remain within the correlation, showing no excess radio emission, suggesting that X-ray emissions in our SMG sample likely originate primarily from star formation.

5.1. The IR-radio correlation factor q_{IR}

Because both far-infrared and radio emission originate from massive stars, galaxies exhibit a remarkably tight linear correlation between their total infrared and 1.4 GHz radio luminosities over several orders of magnitude (Helou et al. 1985)—a relation known as the infrared–radio correlation.

Helou et al. (1985) introduced the parameter q (or q_{FIR}) to quantify the IRRC, defined as the logarithmic ratio of far-infrared flux (42.5–122.5 μm) to 1.4 GHz radio flux (Condon 1992; Yun et al. 2001). However, with evolving observational practices, the correlation is now commonly expressed using the total infrared luminosity (L_{IR} , 8–1000 μm) and the 1.4 GHz radio luminosity (or flux), denoted as q_{IR} (or q_{TIR} , total infrared luminosity). On average, $q_{\text{IR}} = q_{\text{FIR}} + \log_{10}(1.91)$ (Magnelli et al. 2015).

We first calculate the rest-frame 1.4 GHz luminosity, $L_{1.4 \text{ GHz}}$. Using the relation $\nu_{\text{rest}}/\nu_{\text{obs}} = (1+z)$ and $S_{\nu} \propto \nu^{\alpha}$ (radio spectral index α , assumed to be -0.8), we derive the observed 1.4 GHz flux $S_{1.4 \text{ GHz}}^{\text{obs}}$ from the observed 3 GHz flux. Following Ivison et al. (2010), we apply a k -correction factor K to convert $S_{1.4 \text{ GHz}}^{\text{obs}}$ to the rest-frame flux: $K \times S_{1.4 \text{ GHz}}^{\text{obs}}$. Since the observed 1.4

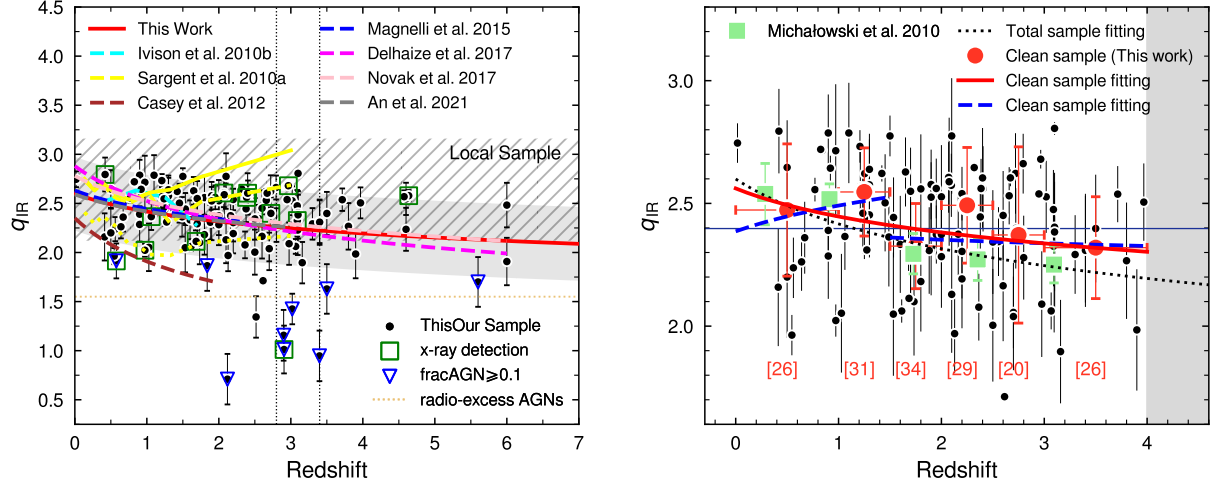


Figure 13. Left: Evolution of the infrared-radio correlation parameter q_{IR} with redshift for the SMG sample. The parameter decreases with redshift as $q_{\text{IR}} \propto (1+z)^{-0.11}$, with a median value of 2.37. The gray shaded region indicates the 1σ uncertainty of the fit, while the hatched band shows the mean and 2σ range for local galaxy sample. Vertical dotted lines delineate the range $z = 3.09 \pm 0.3$, and horizontal dotted line below define as radio-excess AGNs ($q_{\text{IR}} \leq 1.55$; Algera et al. 2020), suggesting that overdense regions may promote galaxy evolution. Right: Evolution of q_{IR} with redshift for the cleaned sample (removing sources with AGN fractions ≥ 0.1 and $z > 4$). Red circles indicate the average q_{IR} in different redshift bins, with the number of sources in each bin shown in brackets. The red solid line shows the fit for the cleaned sample, which is shallower than the full-sample fit (black dotted line). The blue dashed line represents the fit for the cleaned sample split into $z < 1.5$ and $z = 1.5-4$, revealing no strong evolution within these intervals. The overall trend may arise from intrinsic differences between high- and low-redshift SMGs, possibly influenced by downsizing. The horizontal solid line represents the median q_{IR} of total sample.

GHz corresponds to a rest-frame frequency of $1.4(1+z)$ GHz, the k -correction is $K = S_{\nu}^{\text{rest}}/S_{\nu}^{\text{obs}} = \nu^{\alpha}/[\nu(1+z)]^{\alpha} = (1+z)^{-\alpha}$. The rest-frame 1.4 GHz luminosity is then:

$$L_{1.4 \text{ GHz}} = \frac{4\pi D_L^2}{(1+z)^{1+\alpha}} S_{1.4 \text{ GHz}}^{\text{obs}}, \quad (2)$$

where D_L is the luminosity distance in meters. The additional $(1+z)^{-1}$ term accounts for the frequency element interval compression due to cosmological redshift (Murphy et al. 2009; Ivison et al. 2010).

Figure 12 demonstrates the tight relationship between radio (1.4 GHz) and infrared (8-1000 μm) luminosities. A linear regression fit yields: $L_{1.4 \text{ GHz}} [\text{W Hz}^{-1}] = (1.03 \pm 0.05) \times L_{\text{IR}} [\text{W}] + (-16.11 \pm 2.00)$, with a 1σ scatter of 0.38 dex. This result is consistent with that derived from local galaxy samples (Bell 2003), indicating that high-redshift SMGs follow the IRRC and lie at the high-luminosity end. A few outliers are present, most of which are likely due to excess radio emission from AGN activity.

We adopt the q_{IR} definition from Ivison et al. (2010) and Sargent et al. (2010a):

$$q_{\text{IR}} = \log_{10} \left(\frac{L_{\text{IR}} [\text{W}]}{3.75 \times 10^{12} \text{ Hz}} \right) - \log_{10} (L_{1.4 \text{ GHz}} [\text{W Hz}^{-1}]), \quad (3)$$

where L_{IR} is the rest-frame integrated infrared luminosity (8-1000 μm), and $L_{1.4 \text{ GHz}}$ is the rest-frame 1.4 GHz

luminosity. The factor 3.75×10^{12} Hz corresponds to the midpoint frequency of the 42.5-122.5 μm band (Ivison et al. 2010).

In Figure 13, our analysis of the 146 sources jointly detected in the submillimeter and radio bands yields a median IRRC coefficient of $q_{\text{IR}} = 2.37 \pm 0.04$ with a 1σ dispersion of 0.37. The sample exhibits a mild decreasing trend with redshift: $q_{\text{IR}} = (2.60 \pm 0.11) \times (1+z)^{-0.11 \pm 0.04}$.

Blue inverted triangles and green squares in Figure 13 denote sources with an AGN fraction of at least 10% and those detected in X-rays, respectively. The AGN-tagged sources are predominantly outliers, exhibiting excess radio emission (Figure 12) and consequently lower q_{IR} values. These sources fall below or near the radio-excess AGNs threshold (yellow dashed line in Figure 13, $q_{\text{IR}} \leq 1.55$; Algera et al. 2020), while several unmarked sources close to this criterion may also be potential AGN candidates. Interestingly, the sources exhibiting the lowest q_{IR} values are located around $z \sim 3.09$, potentially associated with the SSA22 protocluster (if consider photometric redshift uncertainties $\Delta z \sim 0.3$). This suggests that dense environments may enhance galaxy interactions and/or leverage the abundant gas reservoirs within clusters promote galaxy evolution, thereby boosting AGN activity (Lehmer et al. 2009; Umehata et al. 2015). Among the AGN-flagged sources, only two have

X-ray detections. Most X-ray-detected sources instead display near- or above-average q_{IR} , exhibiting elevated infrared luminosities. This implies that X-ray emission in DSFGs predominantly originates from vigorous star formation (e.g., X-ray binaries) rather than AGN activity.

Compared to local galaxy samples ($q_{\text{IR}} \sim 2.64$; [Yun et al. 2001](#); [Bell 2003](#)), our SMGs show systematically lower values by 0.27 dex, implying either reduced infrared luminosities or enhanced radio emission by a factor of ~ 2 . Nevertheless, the bulk of our SMG population remains within 2σ of the local distribution (shaded region in left panel of Figure 13). These results align well with previous studies of infrared/radio-selected galaxies ([Murphy et al. 2009](#); [Ivison et al. 2009, 2010](#); [Sargent et al. 2010b](#); [Magnelli et al. 2015](#); [Delhaize et al. 2017](#)) and SMG samples ([Murphy et al. 2009](#); [Michałowski et al. 2010](#)), which report median q_{IR} values in the range $\sim 2.34\text{--}2.41$ and redshift evolution slopes between -0.10 and -0.26 . Our findings show particularly close agreement with the large infrared/radio-selected sample of [Magnelli et al. \(2015\)](#); [An et al. \(2021\)](#), sharing similar distributions and evolutionary trends (slope ~ -0.10 to -0.12) at $2.7\text{--}3\sigma$ significance ([Magnelli et al. 2015](#)).

The lower overall q_{IR} distribution and steeper evolution reported by [Casey et al. \(2012\)](#), as they note, may stem from selection biases in their radio-detected sample, which is corroborated by result from radio-detected subsample of [Sargent et al. \(2010b\)](#) (yellow dotted line in left panel of Figure 13). [Sargent et al. \(2010b\)](#) present q_{IR} distributions for samples selected solely in the radio (yellow dotted line), in the infrared (solid line), and via combined detection (dashed line). At $z < 1.5$, the infrared- and combined-selected samples show similar trends, while the radio-selected sample already deviates by ~ 0.3 dex. Notably, the radio-selected results align closely with those of [Casey et al. \(2012\)](#). This confirms that q_{IR} derived from radio-selected samples alone can be significantly biased—systematically lower and exhibiting a steeper evolutionary slope ([Delhaize et al. 2017](#)). At higher redshifts, the discrepancy between the radio-selected and combined-selected samples grows to 0.5 dex or more, while the infrared-selected sample also diverges significantly from the combined sample by ~ 0.3 dex. At same time, the q_{IR} distribution of their combined-detection sample diverges from our results and those in the literature at $z > 1.5$, and the scatter in the data increases with redshift (Table 6 in [Sargent et al. 2010b](#)), likely due to the lack of reliable photometric redshifts in this regime ([Sargent et al. 2010b](#); [Delhaize et al. 2017](#)).

We re-analyzed a sample from the SSA22 deep field, excluding sources likely affected by radio-loud AGN (i.e., those with $\text{fracAGN} \geq 0.1$, mostly outliers) and high-redshift sources ($z > 4$) where detection completeness may be an issue. For this “cleaned sample”, the median q_{IR} is 2.40 ± 0.04 . A fit to this sample yields a redshift evolution slope $\gamma = -0.07 \pm 0.03$ (where $q_{\text{IR}} \propto (1+z)^\gamma$), with a significance of only $\sim 2.2\sigma$. This indicates that, after removing AGN-dominated outliers, the overall evolutionary trend becomes flatter and less significant.

Our results are also consistent with those for SMG samples from [Murphy et al. \(2009\)](#); [Michałowski et al. \(2010\)](#). As illustrated in right panel of Figure 13, the fitting curve of total jointly submillimeter/radio selected sample (the black dotted line) exhibit an excellent agreement with the median q_{IR} distribution reported by [Michałowski et al. \(2010\)](#) (green squares).

[Michałowski et al. \(2010\)](#) noted a significant difference in the median q_{IR} between sources at $z > 1.5$ and $z < 1.5$, despite claiming no strong evolution in SMGs overall. Motivated by this, we derived median q_{IR} values of this cleaned sample in each redshift bin (shown as red circles in right panel of Figure 13). For sources at $z < 1.5$, the median q_{IR} is 2.55 ± 0.07 , close to the local value ([Bell 2003](#)). For the intermediate redshift bin $z = 1.5\text{--}4$, the median q_{IR} is 2.36 ± 0.04 values are in close agreement with [Michałowski et al. \(2010\)](#) (see their Figure 6). Fitting the $z < 1.5$ and $z = 1.5\text{--}4$ subsamples separately yields slopes of 0.06 ± 0.08 and -0.02 ± 0.07 , respectively, suggesting no clear evolution within either bin.

We therefore conclude that the overall evolutionary trend in q_{IR} primarily arises from intrinsic differences between high-redshift SMGs and their lower-redshift ($z < 1.5$) counterparts. Interestingly, $z \sim 1.5$ corresponds to a critical epoch discussed earlier (Sections 4.1 and 4.4): the period when $850 \mu\text{m}$ -selected SMGs begin quenching and downsizing shifts the population toward lower-mass systems. The underlying cause of difference may be that low-redshift SMGs possess intrinsic properties more similar to local galaxies and possibly exhibit additional infrared emission from cirrus components ([Yun et al. 2001](#); [Michałowski et al. 2010](#)), whereas high-redshift systems display distinct characteristics shaped by their extreme star-formation environments. This reinforces the idea that SMGs, selected at a specific wavelength, are not a homogeneous population but encompass a diverse range of galaxies ([Gruppioni & Pozzi 2018](#)); this diversity will be further explored in Section 5.2.

We compare q_{IR} with both radio and infrared luminosities (Figure 14). Our results show that the trend of

q_{IR} with 1.4 GHz radio luminosity ($L_{1.4 \text{ GHz}}$) in SMGs is in good agreement with previous studies (Ivison et al. 2010; Sargent et al. 2010b), and this trend is also observed in nearby galaxies selected in the optical, infrared, and radio bands (Morić et al. 2010). A slight decline in q_{IR} is seen at $L_{1.4 \text{ GHz}} \lesssim 10^{24.5} [\text{W Hz}^{-1}]$, which becomes more pronounced at higher luminosities and drops sharply for sources exceeding $10^{25} [\text{W Hz}^{-1}]$. Most sources above this radio luminosity threshold are flagged as AGN, suggesting that such high radio luminosities are likely dominated by powerful AGNs, which typically exhibit low q_{IR} values. In the highest infrared luminosity bin ($L_{\text{IR}} \sim 10^{39.5} [\text{W}]$), q_{IR} shows a tendency to increase with L_{IR} , consistent with Sargent et al. (2010b). This may indicate the presence of additional infrared emission mechanisms in galaxies with the most extreme star formation activity, or a relatively slower increase in radio emission compared to infrared. At $L_{\text{IR}} \sim 10^{38.2} [\text{W}]$, q_{IR} appears slightly higher than at intermediate luminosities, these sources are predominantly at $z \lesssim 1.5$, potentially reflecting the additional contribution from cirrus emission in low-redshift galaxies (Yun et al. 2001; Michałowski et al. 2010). However, this deviation is not statistically significant, and we conclude that q_{IR} is largely independent of infrared luminosity.

5.1.1. Does the Infrared-Radio Correlation Evolve?

The question of whether q_{IR} truly evolves with redshift remains actively debated.

Sargent et al. (2010b,a) argue that apparent evolutionary trends stem from selection biases rather than intrinsic physical changes. The detection limitation of infrared or radio surveys can introduce biases in high-redshift samples, affecting the observed q_{IR} distribution. For instance, sensitivity limits in the infrared may bias high-redshift samples toward extreme starbursts or AGN-dominated systems, while radio detection limits can increase the fraction of radio-loud AGNs in the sample (Ivison et al. 2010). Additionally, Sargent et al. (2010b) contend that the failure to properly account for confusion from undetected faint sources below the detection threshold has led to the conclusion of IRRC evolution. They assert that the IRRC is essentially invariant out to $z \lesssim 1.4$, although Magnelli et al. (2015) note this conclusion may still be limited by the small number of high-redshift sources available. Some studies report a correlation between q_{IR} and stellar mass, with q_{IR} decreasing as mass increases (Delvecchio et al. 2021; An et al. 2024). Also, (Bell 2003) suggest that the ratio of thermal to non-thermal radio emission may depend on galaxy mass. Delvecchio et al. (2021) propose a

more radical view, suggesting that the apparent redshift evolution of q_{IR} is primarily driven by an incompleteness bias against low-mass galaxies at high redshift. They argue that the IRRC dependence on redshift is weak and that evolution is primarily driven by stellar mass. However, our sample shows no evidence for a dependence of q_{IR} on stellar mass (slope $\theta = -0.05 \pm 0.13$, assuming $q_{\text{IR}} \propto (\log M_*)^\theta$), likely because our sample is dominated by massive systems ($\log(M_*/M_\odot) \sim 10.6\text{--}12$).

Nonetheless, substantial evidence supports genuine q_{IR} evolution, potentially driven by a combination of the following factors.

The most prominent factor may be AGN activity. Studies indicate a substantial AGN fraction within SMG samples (Alexander et al. 2005; Laird et al. 2010; Johnson et al. 2013). Delhaize et al. (2017) find that AGNs exhibit significantly lower q_{IR} values than star-forming galaxies (SFGs), with more luminous AGNs showing even lower q_{IR} and steeper evolutionary trends. As described above, AGN-tagged SMGs typically show excess radio emission and correspondingly lower q_{IR} . Moreover, the majority of SSA22 SMGs have 1.4 GHz luminosities exceeding $10^{22.7} [\text{W Hz}^{-1}]$, a regime where the radio luminosity function is increasingly dominated by AGNs (Ivison et al. 2010). However, does AGN activity always lead to lower q_{IR} ? Murphy et al. (2009); Michałowski et al. (2010); Morić et al. (2010); Sargent et al. (2010b) note that most AGNs actually follow the same IRRC as star-forming galaxies, with q_{IR} values similar to those in the local universe. This implies that q_{IR} is ineffective at distinguishing obscured or radio-quiet AGNs (Murphy et al. 2009).

Ivison et al. (2009, 2010) suggest that radio activity in high-redshift galaxies may be enhanced relative to infrared emission. The efficiency of free-free (bremsstrahlung) cooling for cosmic-ray electrons may increase at high redshift, thereby boosting the contribution of thermal radio emission (Bell 2003), leading to a decrease in q_{IR} with redshift. However, Delhaize et al. (2017) argue that this mechanism alone cannot fully explain the observed trend (under standard assumptions, free-free emission contributes $\sim 10\%$ of the radio flux (Condon 1992)). Bell (2003) note that non-thermal radio emission dominates at low frequencies ($\lesssim 5 \text{ GHz}$), while thermal radio emission becomes more significant at higher frequencies ($\gtrsim 5 \text{ GHz}$). As redshift increases, a fixed observed frequency probes higher rest-frame frequencies. At the typical peak redshift of SMGs ($z \sim 2.6$), the observed 1.4 GHz already corresponds to rest-frame frequencies where thermal emission contributes more substantially. This enhanced free-free

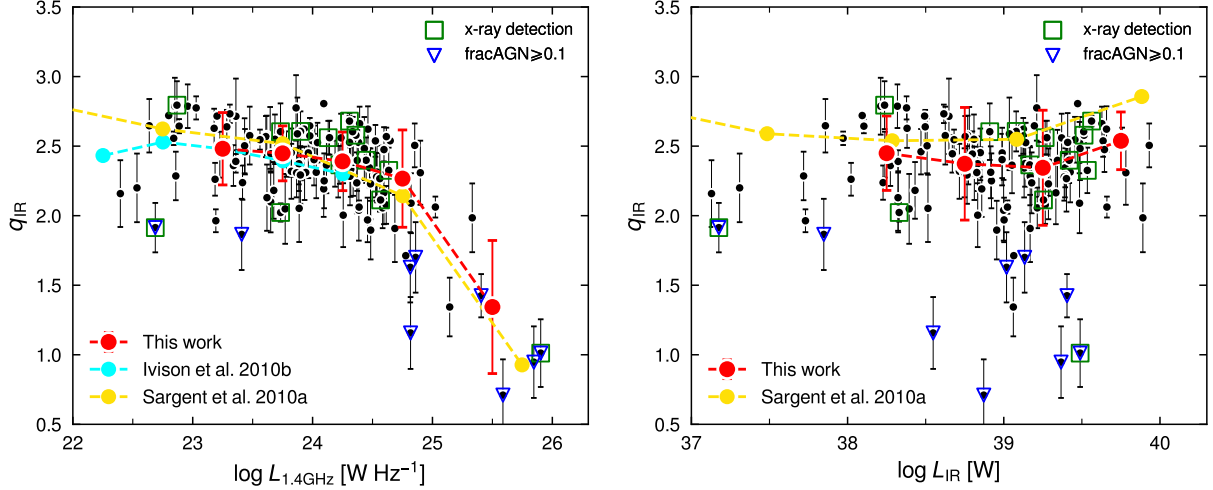


Figure 14. Left: Variation of the q_{IR} with radio luminosity. A weak declining trend is observed, with a rapid decline above $10^{24.5} \text{ W Hz}^{-1}$, suggesting that the most radio-luminous systems are dominated by extremely bright AGNs. Right: Variation of q_{IR} with infrared luminosity. At the brightest luminosity range ($L_{\text{IR}} \gtrsim 10^{39.5} \text{ W}$), q_{IR} increases, possibly indicating additional processes enhancing infrared emission or a relative lag in radio output in extreme starburst environments.

emission increases the total radio luminosity, resulting in a lower q_{IR} .

Physical differences between high-redshift SMGs and local galaxies may lead to different q_{IR} values. High-redshift SMGs are not direct analogs of local ULIRGs (Menéndez-Delmestre et al. 2009). SMGs encompass a diverse population with a wide range of physical properties and a large intrinsic scatter in q_{IR} . Moreover, SMGs host extreme environments and physical processes. For example, Murphy et al. (2009) describe gas “bridges” forming between interacting SMG pairs (interactions and mergers are common in SMGs), which contain significant cosmic-ray electrons and magnetic fields, producing bright radio continuum emission. This radio emission can account for up to half of the system’s total radio output, even before substantial star formation is triggered in the bridge. Such systems exhibit excess radio emission, leading to low q_{IR} values. Additionally, extreme starburst systems in SMGs may possess mechanisms that enhance synchrotron efficiency. Michałowski et al. (2010) suggest that SMGs may be “puffy starbursts” (vertically and radially extended, with scale heights of $\sim 1 \text{ kpc}$), where reduced bremsstrahlung and ionization losses allow cosmic-ray electrons to produce stronger radio emission.

Sample selection biases are also a critical factor that can result in an evolution trend of q_{IR} . Detection limitation mean that radio-selected samples miss radio-faint sources (Ivison et al. 2010), implying that such samples may preferentially include sources with stronger radio emission, leading to systematically lower q_{IR} values (Michałowski et al. 2010). Similarly, high-redshift

infrared-selected samples are biased toward detecting the most luminous infrared galaxies (e.g., ULIRGs) (Sargent et al. 2010b), which may host more extreme star formation or AGN activity. As previously noted, Sargent et al. (2010b) demonstrate significant differences in q_{IR} between samples selected solely by radio, solely by infrared, and by combined detection, with these discrepancies growing at higher redshifts. The results of Casey et al. (2012) support this interpretation. Differences in q_{IR} may also stem from unaccounted mass selection biases. Delvecchio et al. (2021) argue that radio emission exhibits a stronger dependence on stellar mass than infrared emission, with more massive galaxies showing lower q_{IR} . Since SMGs are inherently biased toward massive systems, this could naturally explain differences in q_{IR} compared to local samples. The physical basis for a mass dependence could be that more massive galaxies confine cosmic-ray electrons more effectively, leading to higher non-thermal radio emission relative to their infrared output compared to lower-mass galaxies (Bell 2003). It may also be related to star formation rate surface density (Delvecchio et al. 2021).

Finally, studies suggest that IRRC evolution may also correlate with galactic magnetic field strength, gas density, and star formation rate surface density (Magnelli et al. 2015; Delvecchio et al. 2021; Yoon 2024). Beyond intrinsic physical causes, differences in assumptions and methodologies can also introduce variations in q_{IR} : for example, Delhaize et al. (2017) note that star-forming galaxies may have complex SEDs. Furthermore, assumptions about a fixed radio spectral index, dust emissivity index, and the impact or bias from k -corrections

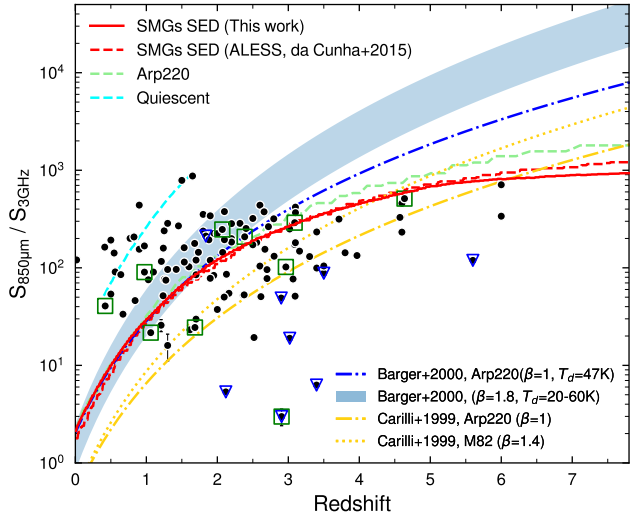


Figure 15. Ratio of submillimeter-to-radio flux as a function of redshift. At low redshifts, SSA22 SMGs show a modest resemblance to templates of quiescent galaxies, though the fit is not particularly tight, while at higher redshifts they approach the ratios of warmer systems like Arp220. Due to the intrinsic diversity of SMGs and the sensitivity of flux ratios to various physical conditions, neither a single template nor the average SMG SED adequately constrains the observed distribution, highlighting limitations in applying generalized models to individual sources.

can all influence the derived q_{IR} values (Murphy et al. 2009).

5.2. Submm/Radio flux ratio

Due to the historical lack of reliable redshift measurements for high-redshift galaxies, several studies have explored the relationship between submillimeter-to-radio flux ratios and redshift as a method for estimating redshifts, known as “millimetric redshifts” (Carilli & Yun 1999; Barger et al. 2000, 2012; Yun et al. 2012). For instance, Carilli & Yun (1999) employed a simple double-power-law model, assuming a constant spectral index in the radio regime and approximating the submillimeter spectrum with an exponential form (Rayleigh-Jeans approximation), adopting submillimeter spectral indices α_s ($= 2 + \beta$, where β is the dust emissivity index) of 3.4 and 3.0 for M82 and Arp220, respectively. Barger et al. (2000) constructed a modified blackbody model based on Arp220 ($\beta = 1$, $T_d = 47\text{K}$). The predictions from these templates are shown in Figure 15.

Additionally, we use templates representing high-redshift SMGs, the local ultraluminous infrared galaxy Arp220, and a local quiescent galaxy (similar to the Milky Way; Chapman et al. 2003) to predict the $850\mu\text{m}/3\text{GHz}$ flux ratio (Figure 15). The predicted flux ratio based on the average SED of SMGs flattens at

higher redshifts. At $z > 4$, the negative k -correction stabilizes the $850\mu\text{m}$ flux, while the rest-frame frequency corresponding to the observed 3 GHz shifts to higher frequencies. Free-free emission begins to dominate the radio spectrum, causing the radio spectral index to flatten and the decrease in radio flux to slow, resulting in an overall flattening of the flux ratio. At even higher redshifts ($z > 7.5$), the rest-frame wavelength corresponding to $850\mu\text{m}$ approaches and then passes the peak of the thermal emission (assuming a dust temperature of 30 K, corresponding to $\sim 100\mu\text{m}$ (Carilli & Yun 1999)), leading to a gradual decline in the submillimeter flux. Consequently, the flux ratio becomes even flatter and even decline.

At low redshifts, SSA22 SMGs appear to show a tendency to be consistent with templates of quiescent galaxies to a moderate degree, while at higher redshifts they approach the hotter Arp220-like systems, despite evidence suggesting SMGs are not simple high-redshift analogs of local ULIRGs. But, our results clearly demonstrate that no single template adequately describes the observed distribution. In contrast to the steep redshift evolution predicted by individual templates, the overall trend of the $S_{850\mu\text{m}}/S_{3\text{GHz}}$ with redshift is relatively flat and can be described by: $S_{850\mu\text{m}}/S_{3\text{GHz}} = (78.83 \pm 23.09) \times (1 + z)^{(0.70 \pm 0.22)}$.

This discrepancy primarily arises from intrinsic diversity of galaxy types among SMGs (Chapman et al. 2005; Casey et al. 2012). Gruppioni & Pozzi (2018) noted that infrared-selected samples encompass galaxies with varied SED shapes, with different shapes dominating infrared emission at different redshifts, making single-template approaches problematic. Even the average SMG SED fails to fully capture the observed scatter, indicating intrinsic SED diversity among SMGs. Furthermore, the average SED represents high-redshift DSFGs and is naturally less suitable for lower-redshift sources. Additionally, the degeneracy between redshift and dust properties—such as varying dust temperatures and emissivities—prevents the submillimeter-to-radio flux ratio from uniquely determining redshift (Blain 1999; Chapman et al. 2005; Casey et al. 2012). As discussed previously, these galaxies may also exhibit dust temperatures that may evolve with redshift (Section 3.2), along with changes in the radio spectral shape at high redshifts (Section 5.1.1). Furthermore, factors such as AGN activity, dust mass and its spatial distribution can also introduce uncertainty.

Therefore, neither a single model nor the average SED of SMGs can tightly constrain the flux ratios of individual SMGs, leading to significant limitations and potentially poor estimation accuracy for individual source.

Nevertheless, due to the relatively concentrated redshift distribution of SMGs, the average SED of SMGs and ULIRGs template remain useful for estimating the mean redshift of a sample (Chapman et al. 2005; Casey et al. 2012).

6. SUMMARY

This paper presents an analysis of the spectral energy distributions, star formation histories, and infrared-radio correlation for 221 850 μm -selected SMGs in the SSA22 deep field (see Paper III). The principal results are summarized as follows:

1. We constructed the average SED for the sample of 221 SMGs (Figure 1). Considerable variation is observed in the optical to near-infrared regimes among individual galaxies. The SED characteristics of SMGs differ from those of typical local ULIRGs or starburst systems, exhibiting cooler dust temperatures. This likely reflects more extended star formation and dust distributions, along with lower mid-infrared dust extinction in SMGs (Menéndez-Delmestre et al. 2009; Symeonidis et al. 2013).
2. SED shapes also vary with evolutionary stage (Figure 1 panel (c)). Quiescent systems display cooler dust and older stellar populations, indicated by a more prominent 1.6 μm bump, stronger Balmer/4000Å breaks, and rising far-UV flux due to the accumulation of low-mass post-AGB stars (Bruzual & Charlot 2003). In contrast, actively starbursting SMGs show stronger dust attenuation and warmer dust temperatures.
3. We provide average SEDs grouped by various physical and observational properties (Figure 2). With increasing redshift, SMGs exhibit higher total luminosity and warmer dust temperatures. Galaxies with greater dust mass tend to have lower infrared luminosity, colder dust, and higher submillimeter flux/luminosity. Higher A_V correlates with stronger overall dust emission but does not systematically alter dust temperature, suggesting that attenuation is governed by multiple physical processes rather than a single mechanism. Because SMGs in different submillimeter flux bins exhibit similar SED shapes, the 850 μm flux alone is insufficient to distinguish between different galaxy types.
4. The majority of SMGs lie at the high-mass end of the star-forming main sequence, with starburst systems comprising $\sim 26\%$ of the sample (Figure 4). We identify a “characteristic stellar mass” of $M_{\text{star}} \sim 10^{11} \text{ M}_{\odot}$, above which SMGs are predominantly on the main sequence or in the quenched phase (Figure 5). At a given evolutionary stage, SMGs at lower redshifts tend to have lower stellar masses than their high-redshift counterparts (Figure 5). The sSFR of SMGs decreases with decreasing redshift (Figure 6), revealing a clear “downsizing” effect: more massive galaxies complete their major mass assembly earlier and quench first, shifting the locus of star formation in the SMG population toward lower-mass systems at later times.
5. We investigated the star formation histories of SMGs (Figure 7). The median mass-weighted age of the sample is 567 Myr, with substantial variation across different evolutionary stages. The majority of quenched SMGs have undergone extended evolutionary histories, averaging ~ 2 Gyr. In contrast, rapidly evolving quenched systems typically experienced two intense, closely spaced starbursts, resulting in a much younger average age of ~ 0.4 Gyr. Starbursting SMGs generally undergo a secondary star formation episode, which contributes significantly to their mass assembly—particularly for those with longer star formation histories. We also identify a minority of massive galaxies that underwent extremely rapid mass assembly in the early universe, with star formation efficiencies reaching ~ 0.2 – 0.8 (Section 4.2).
6. Using mass-weighted stellar ages and gas depletion timescales, we reconstruct the evolutionary timeline of 850 μm -selected SMGs (Figure 8). Most galaxies began forming stars around 1.68 Gyr after the Big Bang and underwent approximately 1 Gyr of evolution before being observed in their “SMG state”. They then exit the SMG phase within roughly 0.2 Gyr of active star formation, subsequently evolving into quiescent, redder systems (Section 4.2.1).
7. Our SMG sample contributes, on average, $\sim 21\%$ to the cosmic SFRD (Figure 9). This fraction peaks at 50–60% in the redshift range $z = 2.5$ – 3.5 , but declines sharply at higher redshifts ($z = 4$ – 6) due to changes in the star formation mode (Zavala et al. 2021). At lower redshifts, the contribution decreases further due to the “downsizing” effect, declining baryonic conversion efficiency, and wavelength selection biases. We also find that SMGs in overdense regions of the field make a significant

contribution to the cosmic infrared background. The sample contributes $\sim 28\%$ to the cosmic SMD, with a redshift evolution trend consistent with its SFRD contribution (Figure 10). The number density of SMGs evolves rapidly from the early universe to $z \sim 1\text{-}3$, increasing from $\sim 3\text{-}4 \times 10^{-6}$ cMpc^{-3} to $\sim 4\text{-}6 \times 10^{-5}$ cMpc^{-3} (Figure 11). At lower redshifts ($z \lesssim 1\text{-}1.5$), $850\,\mu\text{m}$ surveys miss a population of submillimeter-faint galaxies with warmer dust temperatures due to gas exhaustion, downsizing, and bandpass selection effects (Section 4.4).

8. The average infrared–radio correlation parameter q_{IR} for our sample is 2.37, with a mild evolution observed as $q_{\text{IR}} \propto (1+z)^{-0.11}$ (Figure 13). This trend may be influenced by the presence of AGNs at high redshifts. Additionally, the evolution in q_{IR} also arises from intrinsic differences between low- and high-redshift SMGs, potentially linked to the “downsizing” effect or the increasing similarity of low-redshift SMGs to local star-forming galaxies (Section 5.1, Section 5.1.1). The submillimeter-to-radio flux ratio evolves gently as $S_{850\,\mu\text{m}}/S_{3\,\text{GHz}} \propto (1+z)^{0.70}$, and no single SED template adequately captures its distribution—highlighting the intrinsic diversity in SMG spectral shapes (Figure 15).

ACKNOWLEDGMENTS

1 Y.A. acknowledges the support from the National
2 Key R&D Program of China (2023YFA1608204), the
3 National Natural Science Foundation of China (NSFC
4 grant 12173089), and the Strategic Priority Research
5 Program of the Chinese Academy of Sciences (grant
6 No.XDB0800301).

7 The James Clerk Maxwell Telescope is operated by
8 the East Asian Observatory on behalf of The National
9 Astronomical Observatory of Japan; Academia Sinica
10 Institute of Astronomy and Astrophysics; the Korea As-
11 tronomy and Space Science Institute; the National As-
12 tronomical Research Institute of Thailand; Center for
13 Astronomical Mega-Science (as well as the National Key
14 R&D Program of China with No. 2017YFA0402700).
15 Additional funding support is provided by the Science
16 and Technology Facilities Council of the United King-
17 dom and participating universities and organizations in
18 the United Kingdom and Canada. Additional funds
19 for the construction of SCUBA-2 were provided by the
20 Canada Foundation for Innovation.

21 K.M. acknowledges the Waseda University Grant for
22 Special Research Projects (Project number: 2025C-
23 484).

24 *Software:* astropy (Astropy Collaboration et al.
2013, 2018, 2022), pandas (pandas development team
2020), numpy (Harris et al. 2020), matplotlib (Hunter
2007), scipy (Virtanen et al. 2020; Wes McKinney 2010),

APPENDIX

REFERENCES

Aghanim, N., Akrami, Y., Ashdown, M., et al. 2020, A&A, 641, A6, doi: [10.1051/0004-6361/201833910](https://doi.org/10.1051/0004-6361/201833910)

Alaghband-Zadeh, S., Chapman, S. C., Swinbank, A. M., et al. 2012, MNRAS, 424, 2232, doi: [10.1111/j.1365-2966.2012.21386.x](https://doi.org/10.1111/j.1365-2966.2012.21386.x)

Alexander, D. M., Smail, I., Bauer, F. E., et al. 2005, Natur, 434, 738, doi: [10.1038/Natur03473](https://doi.org/10.1038/Natur03473)

Algera, H. S. B., van der Vlugt, D., Hodge, J. A., et al. 2020, ApJ, 903, 139, doi: [10.3847/1538-4357/abb77a](https://doi.org/10.3847/1538-4357/abb77a)

An, F., Simpson, J. M., Smail, I., et al. 2019, ApJ, 886, 48, doi: [10.3847/1538-4357/ab4d53](https://doi.org/10.3847/1538-4357/ab4d53)

An, F., Vaccari, M., Smail, I., et al. 2021, MNRAS, 507, 2643, doi: [10.1093/mnras/stab2290](https://doi.org/10.1093/mnras/stab2290)

An, F., Vaccari, M., Best, P. N., et al. 2024, MNRAS, 528, 5346, doi: [10.1093/mnras/stae364](https://doi.org/10.1093/mnras/stae364)

Ao, Y., Matsuda, Y., Henkel, C., et al. 2017, ApJ, 850, 178

Aravena, M., Boogaard, L., Gómez-López, J., et al. 2020, ApJ, 901, 79, doi: [10.3847/1538-4357/ab99a2](https://doi.org/10.3847/1538-4357/ab99a2)

Arrigoni Battaia, F., Chen, C.-C., Fumagalli, M., et al. 2018, A&A, 620, A202, doi: [10.1051/0004-6361/201834195](https://doi.org/10.1051/0004-6361/201834195)

Astropy Collaboration, Robitaille, T. P., Tollerud, E. J., et al. 2013, *A&A*, 558, A33, doi: [10.1051/0004-6361/201322068](https://doi.org/10.1051/0004-6361/201322068)

Astropy Collaboration, Price-Whelan, A. M., Sipőcz, B. M., et al. 2018, *AJ*, 156, 123, doi: [10.3847/1538-3881/aabc4f](https://doi.org/10.3847/1538-3881/aabc4f)

Astropy Collaboration, Price-Whelan, A. M., Lim, P. L., et al. 2022, *ApJ*, 935, 167, doi: [10.3847/1538-4357/ac7c74](https://doi.org/10.3847/1538-4357/ac7c74)

Barger, A. J., Cowie, L. L., & Richards, E. A. 2000, *AJ*, 119, 2092, doi: [10.1086/301341](https://doi.org/10.1086/301341)

Barger, A. J., Wang, W.-H., Cowie, L. L., et al. 2012, *ApJ*, 761, 89, doi: [10.1088/0004-637X/761/2/89](https://doi.org/10.1088/0004-637X/761/2/89)

Barnes, J. E. 2002, *MNRAS*, 333, 481, doi: [10.1046/j.1365-8711.2002.05335.x](https://doi.org/10.1046/j.1365-8711.2002.05335.x)

Barro, G., Faber, S. M., Pérez-González, P. G., et al. 2013, *ApJ*, 765, 104, doi: [10.1088/0004-637X/765/2/104](https://doi.org/10.1088/0004-637X/765/2/104)

Barro, G., Kriek, M., Pérez-González, P. G., et al. 2017, *ApJL*, 851, L40, doi: [10.3847/2041-8213/aa9f0d](https://doi.org/10.3847/2041-8213/aa9f0d)

Barrufet, L., Pearson, C., Serjeant, S., et al. 2020, *A&A*, 641, A129, doi: [10.1051/0004-6361/202037838](https://doi.org/10.1051/0004-6361/202037838)

Barrufet, L., Oesch, P. A., Marques-Chaves, R., et al. 2025, *MNRAS*, 537, 3453, doi: [10.1093/mnras/staf013](https://doi.org/10.1093/mnras/staf013)

Behroozi, P., Wechsler, R. H., Hearn, A. P., & Conroy, C. 2019, *MNRAS*, 488, 3143, doi: [10.1093/mnras/stz1182](https://doi.org/10.1093/mnras/stz1182)

Behroozi, P. S., Wechsler, R. H., & Conroy, C. 2013, *ApJ*, 770, 57, doi: [10.1088/0004-637X/770/1/57](https://doi.org/10.1088/0004-637X/770/1/57)

Bell, E. F. 2003, *ApJ*, 586, 794, doi: [10.1086/367829](https://doi.org/10.1086/367829)

Birnboim, Y., & Dekel, A. 2003, *MNRAS*, 345, 349, doi: [10.1046/j.1365-8711.2003.06955.x](https://doi.org/10.1046/j.1365-8711.2003.06955.x)

Blain, A. 2002, *PhR*, 369, 111

Blain, A. W. 1999, *MNRAS*, 309, 955, doi: [10.1046/j.1365-8711.1999.02916.x](https://doi.org/10.1046/j.1365-8711.1999.02916.x)

Boquien, M., Burgarella, D., Roehlly, Y., et al. 2019, *A&A*, 622, A103

Bourne, N., Dunlop, J. S., Merlin, E., et al. 2017, *MNRAS*, 467, 1360

Bouwens, R. J., Illingworth, G., Ellis, R. S., Oesch, P., & Stefanon, M. 2022, *ApJ*, 940, 55, doi: [10.3847/1538-4357/ac86d1](https://doi.org/10.3847/1538-4357/ac86d1)

Brammer, G. B., van Dokkum, P. G., & Coppi, P. 2008, *ApJ*, 686, 1503, doi: [10.1086/591786](https://doi.org/10.1086/591786)

Brinchmann, J., & Ellis, R. 2000, *ApJ*, 536, L77, doi: [10.1086/312738](https://doi.org/10.1086/312738)

Bruzual, G., & Charlot, S. 2003, *MNRAS*, 344, 1000

Carilli, C. L., & Yun, M. S. 1999, *ApJ*, 513, L13, doi: [10.1086/311909](https://doi.org/10.1086/311909)

Casey, C. M., Narayanan, D., & Cooray, A. 2014, *PhR*, 541, 45

Casey, C. M., Berta, S., Béthermin, M., et al. 2012, *ApJ*, 761, 140, doi: [10.1088/0004-637X/761/2/140](https://doi.org/10.1088/0004-637X/761/2/140)

Casey, C. M., Zavala, J. A., Manning, S. M., et al. 2021, *ApJ*, 923, 215, doi: [10.3847/1538-4357/ac2eb4](https://doi.org/10.3847/1538-4357/ac2eb4)

Chabrier, G. 2003, *PASP*, 115, 763, doi: [10.1086/376392](https://doi.org/10.1086/376392)

Chan, S.-W., Ao, Y., & Tan, Q.-h. 2025, *ApJ*, 995, 90, doi: [10.3847/1538-4357/ae10a2](https://doi.org/10.3847/1538-4357/ae10a2)

Chapman, S. C., Blain, A. W., Smail, I., & Ivison, R. J. 2005, *ApJ*, 622, 772, doi: [10.1086/428082](https://doi.org/10.1086/428082)

Chapman, S. C., Barger, A. J., Cowie, L. L., et al. 2003, *ApJ*, 585, 57, doi: [10.1086/345980](https://doi.org/10.1086/345980)

Chen, C.-C., Smail, I., Swinbank, A. M., et al. 2015, *ApJ*, 799, 194, doi: [10.1088/0004-637X/799/2/194](https://doi.org/10.1088/0004-637X/799/2/194)

Chen, C.-C., Smail, I., Ivison, R. J., et al. 2016, *ApJ*, 820, 82

Chen, Y. Y., Hirashita, H., Wang, W.-H., & Nakai, N. 2021, *MNRAS*, stab3142, doi: [10.1093/mnras/stab3142](https://doi.org/10.1093/mnras/stab3142)

Clements, D. L., Pearson, C., Farrah, D., et al. 2018, *MNRAS*, 475, 2097, doi: [10.1093/mnras/stx3227](https://doi.org/10.1093/mnras/stx3227)

Condon, J. J. 1992, *ARA&A*, 30, 575

Cowie, L. L., Songaila, A., Hu, E. M., & Cohen, J. G. 1996, *AJ*, 112, 839, doi: [10.1086/118058](https://doi.org/10.1086/118058)

Cowley, W. I., Béthermin, M., del P. Lagos, C., et al. 2017, *MNRAS*, 467, 1231, doi: [10.1093/mnras/stx165](https://doi.org/10.1093/mnras/stx165)

Cunha, E. D., Walter, F., Smail, I. R., et al. 2015, *ApJ*, 806, 110, doi: [10.1088/0004-637X/806/1/110](https://doi.org/10.1088/0004-637X/806/1/110)

Daddi, E., Dickinson, M., Morrison, G., et al. 2007, *ApJ*, 670, 156, doi: [10.1086/521818](https://doi.org/10.1086/521818)

Davé, R., Finlator, K., & Oppenheimer, B. D. 2011, *MNRAS*, 421, 98, doi: [10.1111/j.1365-2966.2011.20148.x](https://doi.org/10.1111/j.1365-2966.2011.20148.x)

Davé, R., Finlator, K., Oppenheimer, B. D., et al. 2010, *MNRAS*, 404, 1355, doi: [10.1111/j.1365-2966.2010.16395.x](https://doi.org/10.1111/j.1365-2966.2010.16395.x)

De Breuck, C., Williams, R. J., Swinbank, M., et al. 2014, *A&A*, 565, A59, doi: [10.1051/0004-6361/201323331](https://doi.org/10.1051/0004-6361/201323331)

Dekel, A., & Birnboim, Y. 2006, *MNRAS*, 368, 2, doi: [10.1111/j.1365-2966.2006.10145.x](https://doi.org/10.1111/j.1365-2966.2006.10145.x)

Dekel, A., & Burkert, A. 2013, *MNRAS*, 438, 1870, doi: [10.1093/mnras/stt2331](https://doi.org/10.1093/mnras/stt2331)

Dekel, A., Sarkar, K. C., Birnboim, Y., Mandelker, N., & Li, Z. 2023, *MNRAS*, 523, 3201, doi: [10.1093/mnras/stad1557](https://doi.org/10.1093/mnras/stad1557)

Delhaize, J., Smolčić, V., Delvecchio, I., et al. 2017, *A&A*, 602, A4, doi: [10.1051/0004-6361/201629430](https://doi.org/10.1051/0004-6361/201629430)

Delvecchio, I., Daddi, E., Sargent, M. T., et al. 2021, *A&A*, 647, A123, doi: [10.1051/0004-6361/202039647](https://doi.org/10.1051/0004-6361/202039647)

Dole, H., Lagache, G., Puget, J.-L., et al. 2006, *A&A*, 451, 417, doi: [10.1051/0004-6361:20054446](https://doi.org/10.1051/0004-6361:20054446)

Draine, B. T., & Li, A. 2007, *ApJ*, 657, 810

Dressler, A. 1980, *ApJ*, 236, 351, doi: [10.1086/157753](https://doi.org/10.1086/157753)

Dudzevičiūtė, U., Smail, I., Swinbank, A. M., et al. 2020, *MNRAS*, 494, 3828

Dunlop, J. S., McLure, R. J., Biggs, A. D., et al. 2017, *MNRAS*, 466, 861, doi: [10.1093/mnras/stw3088](https://doi.org/10.1093/mnras/stw3088)

Eales, S., Lilly, S., Gear, W., et al. 1999, *ApJ*, 515, 518, doi: [10.1086/307069](https://doi.org/10.1086/307069)

Elbaz, D., Dickinson, M., Hwang, H. S., et al. 2011, *A&A*, 533, A119, doi: [10.1051/0004-6361/201117239](https://doi.org/10.1051/0004-6361/201117239)

Engel, H., Tacconi, L. J., Davies, R. I., et al. 2010, *ApJ*, 724, 233, doi: [10.1088/0004-637X/724/1/233](https://doi.org/10.1088/0004-637X/724/1/233)

Euclid Collaboration, Zalesky, L., Weaver, J. R., et al. 2025, Euclid preparation: TBD. Cosmic Dawn Survey: evolution of the galaxy stellar mass function across 0.2, arXiv, doi: [10.48550/ARXIV.2504.17867](https://doi.org/10.48550/ARXIV.2504.17867)

Firmani, C., & Avila-Reese, V. 2010, *ApJ*, 723, 755, doi: [10.1088/0004-637X/723/1/755](https://doi.org/10.1088/0004-637X/723/1/755)

Fitzpatrick, E. 1999, *PASP*, 111, 63

Fujimoto, S., Ouchi, M., Kohno, K., et al. 2018, *ApJ*, 861, 7, doi: [10.3847/1538-4357/aac6c4](https://doi.org/10.3847/1538-4357/aac6c4)

Fujimoto, S., Kohno, K., Ouchi, M., et al. 2024, *ApJS*, 275, 36, doi: [10.3847/1538-4365/ad5ae2](https://doi.org/10.3847/1538-4365/ad5ae2)

Gao, Z.-K., Lim, C.-F., Wang, W.-H., et al. 2024, *ApJ*, 971, 117, doi: [10.3847/1538-4357/ad53c1](https://doi.org/10.3847/1538-4357/ad53c1)

Geach, J. E., Dunlop, J. S., Halpern, M., et al. 2017, *MNRAS*, 465, 1789

Genzel, R., Baker, A. J., Tacconi, L. J., et al. 2003, *ApJ*, 584, 633, doi: [10.1086/345718](https://doi.org/10.1086/345718)

Genzel, R., Newman, S., Jones, T., et al. 2011, *ApJ*, 733, 101, doi: [10.1088/0004-637X/733/2/101](https://doi.org/10.1088/0004-637X/733/2/101)

Gillman, S., Gullberg, B., Brammer, G., et al. 2023, *A&A*, 676, A26, doi: [10.1051/0004-6361/202346531](https://doi.org/10.1051/0004-6361/202346531)

Gillman, S., Smail, I., Gullberg, B., et al. 2024, *A&A*, 691, A299, doi: [10.1051/0004-6361/202451006](https://doi.org/10.1051/0004-6361/202451006)

Girelli, G., Pozzetti, L., Bolzonella, M., et al. 2020, *A&A*, 634, A135, doi: [10.1051/0004-6361/201936329](https://doi.org/10.1051/0004-6361/201936329)

Gottumukkala, R., Barrufet, L., Oesch, P. A., et al. 2024, *MNRAS*, 530, 966, doi: [10.1093/mnras/stae754](https://doi.org/10.1093/mnras/stae754)

Governato, F., Brook, C. B., Brooks, A. M., et al. 2009, *MNRAS*, 398, 312, doi: [10.1111/j.1365-2966.2009.15143.x](https://doi.org/10.1111/j.1365-2966.2009.15143.x)

Gruppioni, C., & Pozzi, F. 2018, *MNRAS*, 483, 1993, doi: [10.1093/mnras/sty3278](https://doi.org/10.1093/mnras/sty3278)

Gruppioni, C., Béthermin, M., Loiacono, F., et al. 2020, *A&A*, 643, A8, doi: [10.1051/0004-6361/202038487](https://doi.org/10.1051/0004-6361/202038487)

Guzman, R., Gallego, J., Koo, D. C., et al. 1997, *ApJ*, 489, 559, doi: [10.1086/304797](https://doi.org/10.1086/304797)

H. Mo, F. v. d. B. . S. W. 2010, *Galaxy Formation and Evolution* (Cambridge University Press), 79

Harikane, Y., Inoue, A. K., Mawatari, K., et al. 2022, *ApJ*, 929, 1, doi: [10.3847/1538-4357/ac53a9](https://doi.org/10.3847/1538-4357/ac53a9)

Harikane, Y., Inoue, A. K., Ellis, R. S., et al. 2025, *ApJ*, 980, 138, doi: [10.3847/1538-4357/ad9b2c](https://doi.org/10.3847/1538-4357/ad9b2c)

Harris, C. R., Millman, K. J., van der Walt, S. J., et al. 2020, *Nature*, 585, 357, doi: [10.1038/s41586-020-2649-2](https://doi.org/10.1038/s41586-020-2649-2)

Helou, G., Soifer, B. T., & Rowan-Robinson, M. 1985, *ApJ*, 298, L7

Hodge, J. A., Swinbank, A. M., Simpson, J. M., et al. 2016, *ApJ*, 833, 103, doi: [10.3847/1538-4357/833/1/103](https://doi.org/10.3847/1538-4357/833/1/103)

Hodge, J. A., da Cunha, E., Kendrew, S., et al. 2025, *ApJ*, 978, 165, doi: [10.3847/1538-4357/ad9a52](https://doi.org/10.3847/1538-4357/ad9a52)

Hopkins, P. F., Cox, T. J., Younger, J. D., & Hernquist, L. 2009, *ApJ*, 691, 1168, doi: [10.1088/0004-637X/691/2/1168](https://doi.org/10.1088/0004-637X/691/2/1168)

Hughes, D. H., Serjeant, S., Dunlop, J., et al. 1998, *Natur*, 394, 241, doi: [10.1038/28328](https://doi.org/10.1038/28328)

Hunter, J. D. 2007, *Computing in Science & Engineering*, 9, 90, doi: [10.1109/MCSE.2007.55](https://doi.org/10.1109/MCSE.2007.55)

Hyun, M., Im, M., Smail, I. R., et al. 2023, *ApJS*, 264, 19

Ivison, R. J., Alexander, D. M., Biggs, A. D., et al. 2009, *MNRAS*, 402, 245, doi: [10.1111/j.1365-2966.2009.15918.x](https://doi.org/10.1111/j.1365-2966.2009.15918.x)

Ivison, R. J., Magnelli, B., Ibar, E., et al. 2010, *A&A*, 518, L31, doi: [10.1051/0004-6361/201014552](https://doi.org/10.1051/0004-6361/201014552)

Johnson, S. P., Wilson, G. W., Wang, Q. D., et al. 2013, *MNRAS*, 431, 662, doi: [10.1093/mnras/stt197](https://doi.org/10.1093/mnras/stt197)

Juneau, S., Glazebrook, K., Crampton, D., et al. 2005, *ApJ*, 619, L135, doi: [10.1086/427937](https://doi.org/10.1086/427937)

Kroupa, P., & Weidner, C. 2003, *ApJ*, 598, 1076, doi: [10.1086/379105](https://doi.org/10.1086/379105)

Laird, E. S., Nandra, K., Pope, A., & Scott, D. 2010, *MNRAS*, 401, 2763, doi: [10.1111/j.1365-2966.2009.15860.x](https://doi.org/10.1111/j.1365-2966.2009.15860.x)

Le Bail, A., Daddi, E., Elbaz, D., et al. 2024, *A&A*, 688, A53, doi: [10.1051/0004-6361/202347465](https://doi.org/10.1051/0004-6361/202347465)

Lehmer, B. D., Alexander, D. M., Geach, J. E., et al. 2009, *ApJ*, 691, 687, doi: [10.1088/0004-637X/691/1/687](https://doi.org/10.1088/0004-637X/691/1/687)

Li, Z., Dekel, A., Sarkar, K. C., et al. 2024, *A&A*, 690, A108, doi: [10.1051/0004-6361/202348727](https://doi.org/10.1051/0004-6361/202348727)

Liao, C.-L., Chen, C.-C., Wang, W.-H., et al. 2024, *ApJ*, 961, 226, doi: [10.3847/1538-4357/ad148c](https://doi.org/10.3847/1538-4357/ad148c)

Lilly, S. J., Eales, S. A., Gear, W. K. P., et al. 1999, *ApJ*, 518, 641, doi: [10.1086/307310](https://doi.org/10.1086/307310)

Lim, C.-F., Wang, W.-H., Smail, I., et al. 2020a, *ApJ*, 889, 80

Lim, C.-F., Chen, C.-C., Smail, I., et al. 2020b, *ApJ*, 895, 104, doi: [10.3847/1538-4357/ab8eaf](https://doi.org/10.3847/1538-4357/ab8eaf)

Liu, D., Daddi, E., Dickinson, M., et al. 2018, *ApJ*, 853, 172

Liu, D., Schinnerer, E., Groves, B., et al. 2019, *ApJ*, 887, 235, doi: [10.3847/1538-4357/ab578d](https://doi.org/10.3847/1538-4357/ab578d)

Liu, F.-Y., Dunlop, J. S., McLure, R. J., et al. 2025, *MNRAS*, 545, doi: [10.1093/mnras/staf1961](https://doi.org/10.1093/mnras/staf1961)

Long, A. S., Casey, C. M., del P. Lagos, C., et al. 2023, *ApJ*, 953, 11, doi: [10.3847/1538-4357/acddde](https://doi.org/10.3847/1538-4357/acddde)

Lonsdale, C. J., Farrah, D., & Smith, H. E. 2006, Ultraluminous Infrared Galaxies (Springer Berlin Heidelberg), 285, doi: [10.1007/3-540-30313-8_9](https://doi.org/10.1007/3-540-30313-8_9)

Madau, P., & Dickinson, M. 2014, *ARA&A*, 52, 415, doi: [10.1146/annurev-astro-081811-125615](https://doi.org/10.1146/annurev-astro-081811-125615)

Magnelli, B., Saintonge, A., Lutz, D., et al. 2012, *A&A*, 548, A22, doi: [10.1051/0004-6361/201220074](https://doi.org/10.1051/0004-6361/201220074)

Magnelli, B., Popesso, P., Berta, S., et al. 2013, *A&A*, 553, A132, doi: [10.1051/0004-6361/201321371](https://doi.org/10.1051/0004-6361/201321371)

Magnelli, B., Lutz, D., Saintonge, A., et al. 2014, *A&A*, 561, A86, doi: [10.1051/0004-6361/201322217](https://doi.org/10.1051/0004-6361/201322217)

Magnelli, B., Ivison, R. J., Lutz, D., et al. 2015, *A&A*, 573, A45, doi: [10.1051/0004-6361/201424937](https://doi.org/10.1051/0004-6361/201424937)

Martig, M., Bournaud, F., Teyssier, R., & Dekel, A. 2009, *ApJ*, 707, 250, doi: [10.1088/0004-637X/707/1/250](https://doi.org/10.1088/0004-637X/707/1/250)

McAlpine, S., Smail, I., Bower, R. G., et al. 2019, *MNRAS*, 488, 2440, doi: [10.1093/mnras/stz1692](https://doi.org/10.1093/mnras/stz1692)

McKinney, J., Casey, C. M., Long, A. S., et al. 2025, *ApJ*, 979, 229, doi: [10.3847/1538-4357/ada357](https://doi.org/10.3847/1538-4357/ada357)

Menéndez-Delmestre, K., Blain, A. W., Swinbank, M., et al. 2013, *ApJ*, 767, 151, doi: [10.1088/0004-637X/767/2/151](https://doi.org/10.1088/0004-637X/767/2/151)

Menéndez-Delmestre, K., Blain, A. W., Smail, I., et al. 2009, *ApJ*, 699, 667

Merlin, E., Chiosi, C., Piovan, L., et al. 2012, *MNRAS*, 427, 1530, doi: [10.1111/j.1365-2966.2012.21965.x](https://doi.org/10.1111/j.1365-2966.2012.21965.x)

Merlin, E., Fortuni, F., Calabró, A., et al. 2025, Witnessing downsizing in the making: quiescent and breathing galaxies at the dawn of the Universe, arXiv, doi: [10.48550/ARXIV.2509.09764](https://doi.org/10.48550/ARXIV.2509.09764)

Michałowski, M. J., Dunlop, J. S., Ivison, R. J., et al. 2012, *MNRAS*, 426, 1845, doi: [10.1111/j.1365-2966.2012.21828.x](https://doi.org/10.1111/j.1365-2966.2012.21828.x)

Michałowski, M., Hjorth, J., & Watson, D. 2010, *A&A*, 514, A67

Michałowski, M. J., Dunlop, J. S., Koprowski, M. P., et al. 2017, *MNRAS*, 469, 492

Miller, T. B., Hayward, C. C., Chapman, S. C., & Behroozi, P. S. 2015, *MNRAS*, 452, 878, doi: [10.1093/mnras/stv1267](https://doi.org/10.1093/mnras/stv1267)

Mitsuhashi, I., Harikane, Y., Bauer, F. E., et al. 2024, *ApJ*, 971, 161, doi: [10.3847/1538-4357/ad5675](https://doi.org/10.3847/1538-4357/ad5675)

Morić, I., Smolčić, V., Kimball, A., et al. 2010, *ApJ*, 724, 779, doi: [10.1088/0004-637x/724/1/779](https://doi.org/10.1088/0004-637x/724/1/779)

Murphy, E. J. 2009, *ApJ*, 706, 482, doi: [10.1088/0004-637x/706/1/482](https://doi.org/10.1088/0004-637x/706/1/482)

Murphy, E. J., Chary, R.-R., Alexander, D. M., et al. 2009, *ApJ*, 698, 1380, doi: [10.1088/0004-637x/698/2/1380](https://doi.org/10.1088/0004-637x/698/2/1380)

Murray, S., Power, C., & Robotham, A. 2013, *A&C*, 3–4, 23, doi: [10.1016/j.ascom.2013.11.001](https://doi.org/10.1016/j.ascom.2013.11.001)

Narayanan, D., Turk, M., Feldmann, R., et al. 2015, *Natur*, 525, 496, doi: [10.1038/Natur15383](https://doi.org/10.1038/Natur15383)

Neistein, E., Van Den Bosch, F. C., & Dekel, A. 2006, *MNRAS*, 372, 933, doi: [10.1111/j.1365-2966.2006.10918.x](https://doi.org/10.1111/j.1365-2966.2006.10918.x)

Nelan, J. E., Smith, R. J., Hudson, M. J., et al. 2005, *ApJ*, 632, 137, doi: [10.1086/431962](https://doi.org/10.1086/431962)

Noeske, K. G., Weiner, B. J., Faber, S. M., et al. 2007a, *ApJ*, 660, L43, doi: [10.1086/517926](https://doi.org/10.1086/517926)

Noeske, K. G., Faber, S. M., Weiner, B. J., et al. 2007b, *ApJ*, 660, L47, doi: [10.1086/517927](https://doi.org/10.1086/517927)

Olsen, K. P., Rasmussen, J., Toft, S., & Zirm, A. W. 2013, *ApJ*, 764, 4, doi: [10.1088/0004-637x/764/1/4](https://doi.org/10.1088/0004-637x/764/1/4)

Oser, L., Ostriker, J. P., Naab, T., Johansson, P. H., & Burkert, A. 2010, *ApJ*, 725, 2312, doi: [10.1088/0004-637X/725/2/2312](https://doi.org/10.1088/0004-637X/725/2/2312)

pandas development team, T. 2020, *pandas-dev/pandas*: Pandas, 1.5.0, Zenodo, doi: [10.5281/zenodo.3509134](https://doi.org/10.5281/zenodo.3509134)

Peng, C. Y., Ho, L. C., Impey, C. D., & Rix, H.-W. 2010, *AJ*, 139, 2097

Pilyugin, L. S., & Thuan, T. X. 2011, *ApJ*, 726, L23, doi: [10.1088/2041-8205/726/2/L23](https://doi.org/10.1088/2041-8205/726/2/L23)

Robertson, B., Bullock, J. S., Cox, T. J., et al. 2006, *ApJ*, 645, 986, doi: [10.1086/504412](https://doi.org/10.1086/504412)

Salpeter, E. E. 1955, *ApJ*, 121, 161, doi: [10.1086/145971](https://doi.org/10.1086/145971)

Salvato, M., Ilbert, O., & Hoyle, B. 2018, *NatAs*, 3, 212, doi: [10.1038/s41550-018-0478-0](https://doi.org/10.1038/s41550-018-0478-0)

Sargent, M. T., Schinnerer, E., Murphy, E., et al. 2010a, *ApJ*, 714, L190, doi: [10.1088/2041-8205/714/2/l190](https://doi.org/10.1088/2041-8205/714/2/l190)

—. 2010b, *ApJS*, 186, 341, doi: [10.1088/0067-0049/186/2/341](https://doi.org/10.1088/0067-0049/186/2/341)

Sawicki, M. 2002, *AJ*, 124, 3050, doi: [10.1086/344682](https://doi.org/10.1086/344682)

Shim, H., Lee, D., Kim, Y., et al. 2022, *MNRAS*, 514, 2915

Shivaei, I., Boogaard, L., Díaz-Santos, T., et al. 2022, *MNRAS*, 514, 1886, doi: [10.1093/mnras/stac1313](https://doi.org/10.1093/mnras/stac1313)

Shuntov, M., McCracken, H. J., Gavazzi, R., et al. 2022, *A&A*, 664, A61, doi: [10.1051/0004-6361/202243136](https://doi.org/10.1051/0004-6361/202243136)

Shuntov, M., Ilbert, O., Toft, S., et al. 2025, *A&A*, 695, A20, doi: [10.1051/0004-6361/202452570](https://doi.org/10.1051/0004-6361/202452570)

Simpson, J. M., Swinbank, A. M., Smail, I., et al. 2014, *ApJ*, 788, 125, doi: [10.1088/0004-637X/788/2/125](https://doi.org/10.1088/0004-637X/788/2/125)

Simpson, J. M., Smail, I., Swinbank, A. M., et al. 2017, *ApJ*, 839, 58, doi: [10.3847/1538-4357/aa65d0](https://doi.org/10.3847/1538-4357/aa65d0)

—. 2019, *ApJ*, 880, 43, doi: [10.3847/1538-4357/ab23ff](https://doi.org/10.3847/1538-4357/ab23ff)

Sommovigo, L., Ferrara, A., Pallottini, A., et al. 2022, *MNRAS*, 513, 3122, doi: [10.1093/mnras/stac302](https://doi.org/10.1093/mnras/stac302)

Speagle, J. S., Steinhardt, C. L., Capak, P. L., & Silverman, J. D. 2014, *ApJS*, 214, 15

Springel, V., & Hernquist, L. 2005, *ApJ*, 622, L9, doi: [10.1086/429486](https://doi.org/10.1086/429486)

Stach, S. M., Dudzevičiūtė, U., Smail, I., et al. 2019, MNRAS, 487, 4648, doi: [10.1093/mnras/stz1536](https://doi.org/10.1093/mnras/stz1536)

Swinbank, A. M., Chapman, S. C., Smail, I., et al. 2006, MNRAS, 371, 465, doi: [10.1111/j.1365-2966.2006.10673.x](https://doi.org/10.1111/j.1365-2966.2006.10673.x)

Swinbank, A. M., Smail, I., Chapman, S. C., et al. 2010, MNRAS, doi: [10.1111/j.1365-2966.2010.16485.x](https://doi.org/10.1111/j.1365-2966.2010.16485.x)

Swinbank, A. M., Papadopoulos, P. P., Cox, P., et al. 2011, ApJ, 742, 11, doi: [10.1088/0004-637x/742/1/11](https://doi.org/10.1088/0004-637x/742/1/11)

Swinbank, A. M., Simpson, J. M., Smail, I., et al. 2014, MNRAS, 438, 1267, doi: [10.1093/mnras/stt2273](https://doi.org/10.1093/mnras/stt2273)

Symeonidis, M., Vaccari, M., Berta, S., et al. 2013, MNRAS, 431, 2317, doi: [10.1093/mnras/stt330](https://doi.org/10.1093/mnras/stt330)

Tamura, Y., Kohno, K., Nakanishi, K., et al. 2009, Natur, 459, 61

Targett, T. A., Dunlop, J. S., Cirasuolo, M., et al. 2013, MNRAS, 432, 2012, doi: [10.1093/mnras/stt482](https://doi.org/10.1093/mnras/stt482)

Thomas, D., Maraston, C., Bender, R., & De Oliveira, C. M. 2005, ApJ, 621, 673, doi: [10.1086/426932](https://doi.org/10.1086/426932)

Toft, S., Smolčić, V., Magnelli, B., et al. 2014, ApJ, 782, 68, doi: [10.1088/0004-637x/782/2/68](https://doi.org/10.1088/0004-637x/782/2/68)

Traina, A., Gruppioni, C., Delvecchio, I., et al. 2024, A&A, 681, A118, doi: [10.1051/0004-6361/202347048](https://doi.org/10.1051/0004-6361/202347048)

Uematsu, R., Ueda, Y., Kohno, K., et al. 2024, ApJ, 965, 108, doi: [10.3847/1538-4357/ad26f7](https://doi.org/10.3847/1538-4357/ad26f7)

Umehata, H., Tamura, Y., Kohno, K., et al. 2015, ApJ, 815, L8

Umehata, H., Fumagalli, M., Smail, I., et al. 2019, Sci, 366, 97

Viero, M. P., Sun, G., Chung, D. T., Moncelsi, L., & Condon, S. S. 2022, MNRAS, 516, L30, doi: [10.1093/mnrasl/slac075](https://doi.org/10.1093/mnrasl/slac075)

Vikaeus, A., Zackrisson, E., Wilkins, S., et al. 2024, MNRAS, 529, 1299

Virtanen, P., Gommers, R., Oliphant, T. E., et al. 2020, Nature Methods, 17, 261, doi: [10.1038/s41592-019-0686-2](https://doi.org/10.1038/s41592-019-0686-2)

Wang, T., Schreiber, C., Elbaz, D., et al. 2019, Natur, 572, 211, doi: [10.1038/s41586-019-1452-4](https://doi.org/10.1038/s41586-019-1452-4)

Wang, T., Sun, H., Zhou, L., et al. 2025, ApJL, 988, L35, doi: [10.3847/2041-8213/adebe7](https://doi.org/10.3847/2041-8213/adebe7)

Wang, W.-H., Lin, W.-C., Lim, C.-F., et al. 2017, ApJ, 850, 37, doi: [10.3847/1538-4357/aa911b](https://doi.org/10.3847/1538-4357/aa911b)

Weaver, J. R., Davidzon, I., Toft, S., et al. 2023, A&A, 677, A184, doi: [10.1051/0004-6361/202245581](https://doi.org/10.1051/0004-6361/202245581)

Wechsler, R. H., & Tinker, J. L. 2018, ARA&A, 56, 435, doi: [10.1146/annurev-astro-081817-051756](https://doi.org/10.1146/annurev-astro-081817-051756)

Wes McKinney. 2010, in Proceedings of the 9th Python in Science Conference, ed. Stéfan van der Walt & Jarrod Millman, 56 – 61, doi: [10.25080/Majora-92bf1922-00a](https://doi.org/10.25080/Majora-92bf1922-00a)

Wilkins, S. M., Lovell, C. C., Irodou, D., et al. 2023, MNRAS, 527, 7965, doi: [10.1093/mnras/stad3558](https://doi.org/10.1093/mnras/stad3558)

Williams, C. C., Alberts, S., Ji, Z., et al. 2024, ApJ, 968, 34, doi: [10.3847/1538-4357/ad3f17](https://doi.org/10.3847/1538-4357/ad3f17)

Xiao, M., Oesch, P. A., Elbaz, D., et al. 2024, Natur, 635, 311, doi: [10.1038/s41586-024-08094-5](https://doi.org/10.1038/s41586-024-08094-5)

XSMT Project Collaboration Group, Ao, Y., Chang, J., et al. 2025, Scientific Objectives of the Xue-shan-mu-chang 15-meter Submillimeter Telescope, arXiv, doi: [10.48550/ARXIV.2509.13983](https://doi.org/10.48550/ARXIV.2509.13983)

Yamaguchi, Y., Kohno, K., Hatsukade, B., et al. 2020, PASJ, 72, 69, doi: [10.1093/pasj/psaa057](https://doi.org/10.1093/pasj/psaa057)

Yoon, I. 2024, ApJ, 975, 15, doi: [10.3847/1538-4357/ad7385](https://doi.org/10.3847/1538-4357/ad7385)

Yun, M. S., Reddy, N. A., & Condon, J. J. 2001, ApJ, 554, 803, doi: [10.1086/323145](https://doi.org/10.1086/323145)

Yun, M. S., Scott, K. S., Guo, Y., et al. 2012, MNRAS, 420, 957, doi: [10.1111/j.1365-2966.2011.19898.x](https://doi.org/10.1111/j.1365-2966.2011.19898.x)

Zavala, J. A., Aretxaga, I., & Hughes, D. H. 2014, MNRAS, 443, 2384, doi: [10.1093/mnras/stu1330](https://doi.org/10.1093/mnras/stu1330)

Zavala, J. A., Aretxaga, I., Dunlop, J. S., et al. 2018, MNRAS, 475, 5585, doi: [10.1093/mnras/sty217](https://doi.org/10.1093/mnras/sty217)

Zavala, J. A., Casey, C. M., Manning, S. M., et al. 2021, ApJ, 909, 165, doi: [10.3847/1538-4357/abdb27](https://doi.org/10.3847/1538-4357/abdb27)

Zeng, X., Ao, Y., & Zhang, Y. 2024, MNRAS, 528, 2964

Zhang, Y., Zheng, X. Z., Shi, D. D., et al. 2022, MNRAS, 512, 4893, doi: [10.1093/mnras/stac824](https://doi.org/10.1093/mnras/stac824)

Zhang, Y. H., Dannerbauer, H., Pérez-Martínez, J. M., et al. 2024, A&A, 692, A22, doi: [10.1051/0004-6361/202451379](https://doi.org/10.1051/0004-6361/202451379)

—. 2025, JWST reveals extended stellar disks for ALMA-bright dusty star-forming galaxies in the Spiderweb protocluster, arXiv, doi: [10.48550/ARXIV.2512.07050](https://doi.org/10.48550/ARXIV.2512.07050)